Chapter 4

OBSERVATION

Hereafter, we analyze the *ASCA* data of ULXs, in order to reveal their nature. In this chapter, we select targets, describe their *ASCA* observations, and summarize their properties so far reported.

4.1 Sample Selection

The first step of studying ULXs is to select targets. As mentioned in § 2.6, the spectral analysis have already been performed by several authors on some ULXs observed with *ASCA*. However, the attempted spectral models, as well as the utilized detector response functions, vary from authors to authors. Moreover, although some ULXs have been observed twice or more, only the result of the first observation has been published for most of them. We hence analyze not only the unreported sources, but also those for which the results of the spectral analysis have already been published, in order to obtain a unified understanding of ULXs.

By 1999 April, about 100 galaxies (not including AGNs) had been observed by *ASCA*. We first selected galaxies based on Table 2.1, a list of ULXs observed by *Einstein*, taking advantage of its high spatial resolution. Fortunately, all of the galaxies tabulated in Table 2.1 had been observed by *ASCA* and their data were available; they are either in archive, or accessible by the present author because he is included as a co-investigator. Among them, we chose galaxies where ULXs are clearly separated from neighboring sources in the ASCA image, in order to obtain the spectra free from contamination. We hence excluded galaxies having complex X-ray morphology, i.e., NGC 3034 (M82), NGC 4258, NGC 5194 (M51), NGC 5236 (M83), and NGC 5457 (M101). Next we searched galaxies, from the remaining ones, which host off-nucleus luminous sources in the *ASCA* image. After excluding elliptical and S0 galaxies as well as spirals which host an LLAGN, ∼20 spirals remained to be promising. We performed visual inspection on these galaxies, and picked up Dwingeloo 1 and NGC 4565; both had already been reported to host ULXs by Reynolds et al. (1997) and Mizuno et al. (1999). We also included NGC 1365 to our sample galaxies. Although this galaxy hosts an LLAGN, a newly appeared luminous source can be separated from the nucleus in the *ASCA* image, as reported by Iyomoto et al. (1998).

As mentioned in § 2.5.3, one of the possible explanations of ULXs is X-ray bright SNRs. Thus, we also analyze X-ray luminous SNRs for comparison. Among our sample galaxies, NGC 1313 hosts an X-ray luminous SNR, SN 1978K, and NGC 6946 has the

brightest source at its north-arm region, which were identified as an SNR based on the positional coincidence by Schlegel et al. (1994). We also added NGC 891 to our sample galaxies, since this object is known to have X-ray luminous SNR, SN 1986J (Houck et al. 1998). Hereafter we analyze these SNRs as well as ULXs. In § 6.9, we compare spectral properties of ULXs with those of the securely identified extragalactic SNRs, to investigate whether they have common properties or not. All of our sample galaxies are summarized in Table 4.1, and the properties of host galaxies as well as those of involved ULXs (and SNRs) are mentioned in the next subsection.

We end this section by describing the sample completeness. As already mentioned above, the number of galaxies (without AGN) *ASCA* has already observed is up to only ∼100, apparently much smaller than that of galaxies themselves; e.g., in a catalogue of Tully (1988), ∼ 800 galaxies located within 20 Mpc are listed. In addition, *ASCA* observation is usually based on the X-ray detection of the targets by the previous missions such as *Einstein* and *ROSAT*. Hence, *ASCA* observations of galaxy cannot be either complete or unbiased. However, our selection of ULXs is mostly based on the observation by *Einstein Observatory*. This was the first X-ray satellite with imaging instruments, so that its sample selection was relatively unbiased. We therefore regard our sample objects as a relatively good representation of whole ULXs, although we do not claim the completeness of our sample.

Table 4.1: *ASCA* observational log of the host galaxies

Galaxy	Type[a]	Distance[b] (Mpc)	Galactic $N_{\rm H}$ (10^{22}cm^{-2})	Date[c] yymmdd	Exposure (ks)[d] SIS	GIS	SIS Mode[e]	SIS Clock[e]
NGC 598 (M33)	Scd	0.72	0.06	93 07 22	15.4	17.4	F/B	1111/1111
				93 07 23	14.6	17.7	F/B	1111/1111
NGC 891	Sb	9.6	0.07	94 01 21	44.7	49.0	F/B	1100/1100
				96 01 29	51.7	56.2	F/F	0100/0100
NGC 1313	Sd	4.5	0.035	93 07 12	21.2	27.7	F/B	1111/1111
				95 11 29	33.2	32.9	F/F	0100/0100
NGC 1365	Sb	18.3	0.014	94 08 12	8.1	9.1	F/F	0100/0100
				95 01 25	34.0	36.9	F/B	1111/1111
NGC 2403	Scd	3.2	0.04	97 10 29	26.5	29.1	F/B	1100/1100
NGC 3031 (M81)	Sab	3.6	0.04	94 04 01	31.6	37.6	F/F	1000/1000
				94 10 21	37.4	46.0	F/F	0010/0010
				95 04 01	17.6	19.7	F/F	1000/1000
				95 10 24	34.5	37.3	F/F	0010/0010
				96 04 16	43.2	47.7	F/F	1000/1000
				96 10 27	27.8	31.0	F/F	0010/0010
				97 05 08	41.0	48.9	F/F	1000/1000
NGC 3628	Sb	7.7	0.02	93 12 12	21.0	23.1	B/B	1111/1111
NGC 4565	Sb	10.4	0.013	94 05 28	30.8	34.5	F/F	1100/1100
NGC 6946	Scd	5.5	0.2	93 05 31	20.6	26.4	F/B	1111/1111
				94 12 28	102.8	118.9	F/F	1100/0100
IC 342	Scd	3.9	0.3	93 09 19	35.8	38.4	F/B	1111/1111
Dwingeloo 1	Sbc	3.0	0.7	95 09 14	36.1	38.9	F/F	0100/0100

[a] Taken from Tully (1988) except for Dwingeloo 1, which is classified as Sb or Sc by Kraan-Korteweg et al. (1994).
[b] The distance is taken from de Vaucouleurs (1963) for NGC 1313, Madore et al. (1996) for NGC 1365, Freedman & Madore (1988) for NGC 2403, Freedman et al. (1994) for M81, and Tully (1988) for all other galaxies except for NGC 4565, for which we adopted the weighted mean of three independent distance indicators after Mizuno et al. (1999). (see § 7.3.1)
[c] Observation start date. Although M81 have been observed 18 times till today, we utilized the last seven observations whose data is archived in 1999 April (see also § 6.4). Thus we tabulate here only these seven observations.
[d] An average of two SIS sensors or two GIS sensors, after the data screenings (§ 5) are applied.
[e] Clocking mode of S0 for Bit-H/Bit-M.
Note. — GIS bit assignment for Bit-H/Bit-M (PH-X-Y-RT-SP-Time) is 8-8-8-0-0-7/8-8-8-0-0-7 for NGC 1313 in the 1995 observation, and 8-8-8-0-0-7/8-6-6-0-0-10 for M81 in the last three observations.

4.2 Properties of Our Sample Objects

NGC 598 As already mentioned in §2, this galaxy has the brightest source in the Local Group galaxies at its nucleus, namely M33 X-8, and Takano et al. (1994) analyzed the spectra of this ULXs obtained with ASCA. They discovered that its spectra are well represented by the power-law plus MCD model of $T_{\rm in}$∼1 keV, and suggested that the source is a close binary system containing a black hole of $\sim 10 M_\odot$ (§ 2.6.1). We re-analyze its spectra in § 6.3.

NGC 891 This galaxy is an almost perfectly edge-on spiral like NGC 4565. SN 1986J was first discovered in the radio band (Rupen et al. 1987), and its first X-ray observation was performed in 1991 by *ROSAT*. Houck et al. (1998) reported, based on its X-ray data obtained by *ROSAT* and *ASCA*, that the supernova flux decreased in proportion to t^{-2}. They also detected Fe-K line at ∼6.7 keV in the spectrum obtained with *ASCA*. We re-analyze the *ASCA* spectra of SN 1986J in § 6.9 together with other luminous SNRs.

NGC 1313 This is a nearby face-on, late-type Sb galaxy at a distance of 4.5 Mpc (Vaucouleurs 1963). X-ray observations using *Einstein Observatory*, *ROSAT*, and *ASCA* (Fabbiano & Trinchieri 1987; Colbert et al. 1995; Mirrer et al. 1998; Petre et al. 1994) showed that its X-ray emission is dominated by three extremely luminous point-like sources of $L_{\rm X} \sim 10^{39}$erg s^{-1} each. One of them is an X-ray luminous supernova, namely SN 1978K. We call the other two ULXs as source A and source B after Petre et al. (1994), the former located close (∼45″) to the galaxy nucleus. We describe source A and source B in § 6.6 and § 6.5, respectively, and SN 1978K in § 6.9.

NGC 1365 This is a bright barred spiral galaxy in the Fornax cluster. Silbermann et al. (1999) estimated the distance to be 18.3 Mpc by observing its Cepheids with the Hubble Space Telescope (HST). Iyomoto et al. (1997) observed this galaxy twice with *ASCA*. They detected Fe-line emission from the nucleus, and confirmed that this galaxy hosts an obscured AGN. They also reported that a very luminous source of $L_{\rm X}$ ∼10^{40}erg s^{-1} newly appeared in the second observation, located at the south-west of the nucleus with a separation of ∼1′.2. Komossa and Schulz (1998) studied long-term variability of this source with *ROSAT*. We focus on the newly discovered SW source, and re-analyze its spectrum in § 6.8.

NGC 2403 The nearby Sc galaxy NGC 2403 is a member of the M81 group (Tamman & Sandage 1968). The distance to this galaxy was estimated to be ∼ 3.2 Mpc by observing its Cepheids (Freedman and Madore 1988). With the *Einstein Observatory* Fabbiano & Trinchieri (1987) detected three point-like sources of $L_{\rm X} = 10^{38-39}$ erg s^{-1}, called source 1, source 2, and source 3. We analyze the *ASCA* spectrum of the brightest one, source 3, in § 6.8.

NGC 3031 (M81) This object is a nearby early-type spiral galaxy with a prominent bulge and well-defined spiral arms, and has a Cepheid-based accurate distance of 3.6 Mpc from the HST observations (Freedman et al. 1994). Fabbiano (1988) observed this galaxy with *Einstein* and detected several sources, including the brightest one, called X-5, at the nucleus. Using *ASCA*, Ishisaki et al. (1996) confirmed that X-5

is a typical LLAGN of $L_X \sim 10^{40}$ erg s^{-1}, exhibiting a hard power-law continuum and a weak Fe-K line. The most luminous off-nucleus source is called X-6, and has a luminosity of $L_X \sim 1 \times 10^{39}$ erg s^{-1}. Uno (1996) reported that its spectrum in the 1994 observation can be represented by an MCD model of $T_{in} \sim 1.5$ keV. Due to the explosion of SN 1993J in M81, *ASCA* has frequently observed the M81 region (Kohmura et al. 1994; Kohmura 1994; Uno 1997). We analyze the spectra of M81 X-6 in § 6.4, particularly focusing on its long-term variability.

NGC 3628 This galaxy, a member of the Leo Triplet of galaxies, is viewed nearly edge-on ($\sim 80^\circ$) and classified as a starburst galaxy on the basis of its strong, warm far-infrared emission (Rice et al. 1988). Fabbiano et al. (1990) observed this galaxy with *Einstein* and detected an off-nucleus source with $L_X \geq 10^{39}$erg s^{-1}. Yaqoob et al. (1995) obtained the spectrum of this source with *ASCA*, and reported that it can be represented by a power-law model of $\Gamma \geq 2$. We re-analyze this ULX in § 6.8.

NGC 4565 This object, a member of the Coma I group, is an almost perfectly edge-on Sb galaxy similar in size to M31 and the Milky Way. Observation with *ROSAT* revealed two strong point-like sources of $L_X \geq 10^{39}$ erg s^{-1}, one at the nucleus while the other $\sim 1'$ above the disk (Volger et al. 1996). Mizuno et al. (1999) showed that their spectra can be represented by an MCD model of $T_{in} \sim 1.5$ keV. They argued that both objects are ULXs, even though one of them apparently coincides in position with the nucleus (§ 6.7).

NGC 6946 This is a face-on Scd galaxy and hosts a bright starburst nucleus (e.g., Telesco, Harper 1980). In X-rays this galaxy has a strong ($\geq 10^{39}$erg s^{-1}) point-like source on its north arm (Fabbiano & Trinchieri 1987). Schlegel et al. (1994) observed the galaxy with *ROSAT* and identified this source as an X-ray luminous SNR based on the positional coincidence. We analyze its spectrum in § 6.9, together with SN 1986J in NGC 891 and SN 1978K in NGC 1313.

IC 342 This is a nearby starburst Scd galaxy, located close to the Galactic plane ($b \sim 10^\circ$). Fabbiano and Trinchieri (1987) observed it with *Einstein* and showed that its X-ray emission is dominated by three luminous point-like sources with $L_X \geq 10^{39}$ erg s^{-1}, called source 1, source 2, and source 3. Okada et al. (1998) obtained the 0.5–10 keV spectra of these sources and detected short-term variability from source 1, as mentioned in § 2.6.2. The central source, namely source 3, has been resolved into three separate sources in the *ROSAT* HRI image (Bregman et al. 1993, see also the image in Appendix C). Accordingly, we re-analyze the other two sources in this thesis; source 1 in § 6.2 and source 2 in § 6.8.

item[Dwingeloo 1] Kraan–Korteweg et al. (1994) newly discovered a spiral galaxy behind the Milky Way, namely Dwingeloo 1. Reynolds et al. (1997) observed this galaxy in 1995 for the first time in X-rays with *ASCA*, and found an off-center source (Dwingeloo 1 X-1) with $L_X \sim 10^{39}$erg s^{-1}. We treat this ULXs in § 6.8.

Chapter 5

X-RAY IMAGES AND LIGHT CURVES OF ULXS

5.1 X-Ray Images of ULXs

In this section, we describe the reduction processes applied for the *ASCA* data, and investigate the obtained images to identify the involved ULXs. In order to study the source extent, we also use the *ROSAT* HRI data taking advantage of its high ($\leq 10''$) spatial resolution.

5.1.1 Reduction of the *ASCA* images

The original *ASCA* data collected on-board includes several types of false events that should be rejected in the course of data analysis to achieve a good signal-to-noise ratio. In most cases in this thesis, the screening process applied for the data is the same. Therefore we explain the process, applied for the data of NGC 1313 in the 1993 observation, as an example.

As mentioned in Chapter 3, the SIS data are contaminated by hot and flickering pixels. Figure 5.1a is the original SIS 0 image of NGC 1313 in the 0.5–10 keV energy band obtained in 1993 July. We can see hot and flickering pixels as black spots in the image, which obscure the real X-ray sources in the galaxy. These hot and flickering pixels can be removed by comparing the number of events with those of surrounding pixels (§ 3.3.3). Figure 5.1b is the image after removing the hot and flickering pixels.

Next, in order to achieve a good signal-to-noise ratio, the data should be screened to avoid the periods when the background level is uncomfortably high. This process is done by utilizing the orbital information of the satellite. In fact, we applied the following data-screening criteria:

1. The time after passage through the South Atlantic Anomaly (SAA) should be larger than 1 minute.

2. The object should be at least 10° above the night Earth's limb. This is because the Earth's outer atmosphere absorbs and/or scatters X-rays, hence distorts the spectrum.

3. The object should be at least 20° above the bright Earth's limb, since the SIS has sensitivity not only to X-rays but also to optical and UV radiation, due to a particle damage to the optical blocking filter.

4. The cutoff rigidity (COR) of cosmic rays should be larger than 6 GeV/c.

5. The time after day/night transition should be greater than 100 s. This is because the dark-frame level changes so rapidly when the satellite crosses the day/night boundary that the calculation of the dark level becomes wrong (see § 3.3.3).

Finally, the grade selection (§ 3.3.2) was applied to remove the remaining particle events. Figure 5.1c is the obtained SIS 0 image, where three sources are visible. We can see a significant improvement in signal-to-noise ratio.

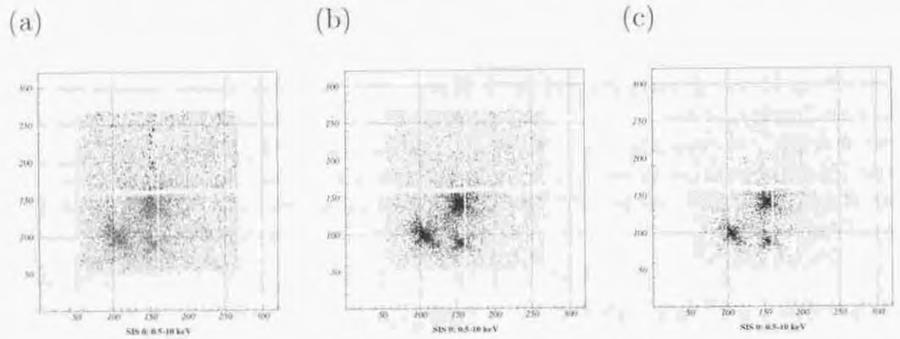

Figure 5.1: SIS 0 image of NGC 1313 in the 0.5–10 keV band, observed in 1993 July. (a) The original image. (b) The image obtained after removing the hot and flickering pixels. (c) The finally obtained image after applying the data selection utilizing the orbital information and grade selection.

For the GIS, we first show in Figure 5.2a the image only after masking the calibration source and the detector rim, where the background level is high. The screening criteria are slightly looser than those of the SIS. Specifically, we applied the following criteria.

1. The time after the SAA passage should be larger than 1 minute.

2. The object should be at least 10° above the Earth's limb.

3. The COR should be greater than 6 GeV/c.

As described in § 3.5, the on-board rise-time screening is relatively coarse. Thus, to remove the remaining particle events, we applied the tighter rise-time rejection, as well as the spread discrimination. The finally obtained image is shown in Figure 5.2b, which reveals the same three sources as detected with the SIS.

We summed thus obtained two SIS (SIS 0 and SIS 1) images into a single SIS image, and two GIS (GIS 2 and GIS 3) images into a single GIS image, and show them in

Figure 5.3b and 5.3c, each superposed on the optical image. There, three strong X-ray sources, corresponding to source A, source B, and SN 1978K, are seen. For other galaxies, we summarize the *ASCA* images in Appendix C. All ULXs of our interest are clearly seen in the *ASCA* SIS and/or GIS images.

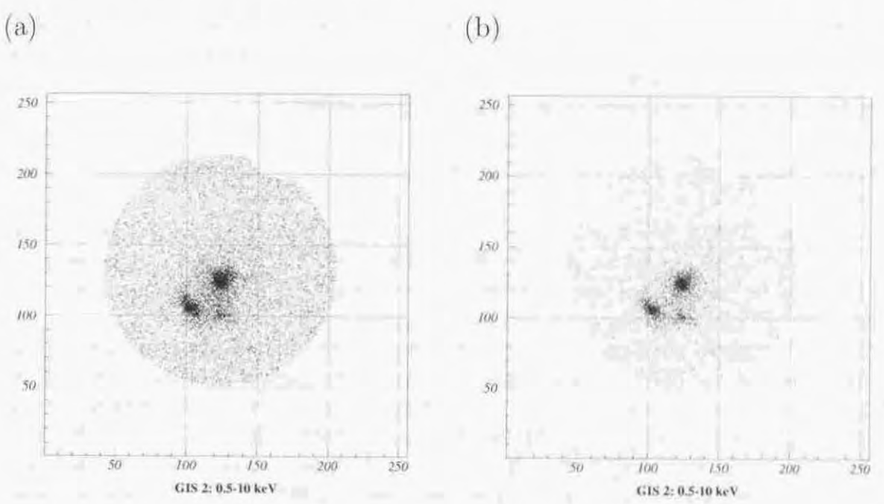

Figure 5.2: GIS 2 image of NGC 1313 in the 0.5–10 keV band, observed in 1993 July. (a) The original image only after masking the calibration source and the detector rim. (b) The finally obtained image after applying the data selection utilizing the orbital information, rise-time rejection, and spread discrimination.

5.1.2 *ROSAT* HRI observations

Although the ULXs are clearly detected in the *ASCA* images (Appendix C), the angular resolution of *ASCA* is far too insufficient to perform meaningful examinations whether they are really pointlike or not. The *ROSAT* HRI, having an order of magnitude higher angular resolution, is much more suited for constraining the angular size of the ULXs. We therefore investigate the archival *ROSAT* HRI data, on which the standard data reduction (e.g., exclusion of the periods of high background counts, earth occultations, and so on) has already been performed. Except for Dwingeloo 1, all of our sample galaxies were observed with the HRI. Some galaxies were observed more than once. However, for each ULX we here utilize the data from one observation only, because superposition of images taken on different occasions might degrade the angular resolution due to possible errors in the aspect solution.

The log of the HRI observations, which we utilized here, is summarized in Table 5.1. We show the HRI image of NGC 1313 in Figure 5.3a, and those of other galaxies in Appendix C. Thus, each of the ULXs (or SNRs) seen in the *ASCA* images corresponds to

a single, point-like source in the HRI image. Further investigation of the source extent is performed in the next subsection.

5.1.3 Studying the source extent

To quantitatively examine the angular extent of the ULXs in the HRI images, we made radial intensity profiles of the individual sources within the radius of 20″, and compared each of them with the HRI point spread function (PSF). The analytic formula of the in-flight, on-axis, nominal PSF of the *ROSAT* HRI is given as

$$A_1 \exp\left[-0.5\left(\frac{r}{\sigma_1}\right)^2\right] + A_2 \exp\left[-0.5\left(\frac{r}{\sigma_2}\right)^2\right] + A_3 \exp\left[-\frac{r}{\sigma_3}\right] \quad \text{(counts/pixel)} \quad , \quad (5.1)$$

(David et al. 1999), where r denotes the radius from the source center, $A_1 = 0.96$, $\sigma_1 = 2.''2$, $A_2 = 0.18$, $\sigma_2 = 4.''0$, $A_3 = 0.0009$, and $\sigma_3 = 31.''7$. The position dependence of the PSF can be neglected if the source is located within $\sim 5'$ from the optical axis (e.g. Boese 1998). Therefore, equation 5.1 is valid for all of our objects.

The PSF formula given by equation 5.1 corresponds to an ideal observation of a point source (David et al. 1999). Due to random errors of the aspect solution, however, the PSF usually becomes wider in actual observations. These effects can be expressed by introducing an additional broadening factor $\sigma_{\rm add}$, and replacing σ_1 in equation 5.1 with $\sqrt{\sigma_1^2 + \sigma_{\rm add}^2}$ and σ_2 with $\sqrt{\sigma_2^2 + \sigma_{\rm add}^2}$. This $\sigma_{\rm add}$ usually takes values of $2'' - 3''$ even for a point source (e.g., Morse 1994; Boese 1998; David et al. 1999). If the source is extended, $\sigma_{\rm add}$ increases beyond these values.

In order to estimate $\sigma_{\rm add}$ for our objects, we fitted the radial profiles with the modified PSF plus a constant background, with $\sigma_{\rm add}$, the PSF normalization, and the background left free. The fitting results are shown in Table 5.2 and Figure 5.4. For most cases, the fit has been acceptable and $\sigma_{\rm add}$ turned out to be $\sim 1.''5 - 3.''5$, implying that the objects can be regarded as point sources. Only for M33 X-8 the fit failed (χ^2/ν=85.3/17), because of significant residuals around the source center. This may be due to contamination of diffuse emission around the nucleus (Schulman and Bregman 1995). We therefore replaced the constant background with a Gaussian distribution, to represent this diffuse emission, and re-fitted the profile. Now, the fit became acceptable (χ^2/ν=22.6/16), and the modification of the PSF turned out to be $\sigma_{\rm add} = 2.''2 \pm 0.''1$, which is again comparable to that of a point source. The diffuse emission is expressed with a Gaussian of $\sigma = 8.''6 \pm 0.''5$, and its contribution to the total events within 20″ is estimated to be only $\sim 13\%$.

Since the source counts of two ULXs in NGC 4565 and NGC 1365 SW-source are insufficient for a reliable fitting, we made image projections instead of radial profiles. For NGC 4565, we projected the events within a $25'' \times 100''$ rectangle region on the line connecting the two sources, and for NGC 1365 SW-source, we projected the events within $25'' \times 25''$ square region. They are also shown in Figure 5.4, where the two sources in NGC 4565 are clearly separated and the widths of the projected profile are $\sim 10''$ in FWHM. Therefore, the X-ray extent is similar to those of other sources. NGC 1365 SW-source was also point-like to the HRI, although its signal counts are quite low (~ 20). Therefore, we regard all these sources studied here to be consistent with point sources within the spatial resolution of the *ROSAT* HRI. Although Dwingeloo 1 X-1 has not been observed by HRI, Reynolds et al. (1997) already confirmed it to be point-like within the spatial resolution of *ASCA*.

Table 5.1: *ROSAT* HRI observational log of the galaxies. Only the observations utilized here are tabulated.

Galaxy	Date (yymmdd)	Exposure (ks)
NGC 598 (M33)	96 01 18	46
NGC 891	95 01 26	98
NGC 1313	94 06 23	22
NGC 1365	94 07 20	10
NGC 2403	95 09 18	26
NGC 3031 (M81)	97 09 30	20
NGC 3628	91 12 07	14
NGC 4565	95 07 05	5.3
NGC 6946	94 05 14	60
IC 342	91 02 13	19

Table 5.2: Estimates of the X-ray extent of our sample objects, using *ROSAT* HIR data. Sources are fitted with a modified PSF plus a constant background (see text). Only for M33 X-8, the constant background is replaced with a gaussian distribution, to represent the diffuse emission. Due to the aspect errors, $\sigma_{\rm add}$=2″–3″ is usually required even for a point source (Morse 1994, Boese 1998, David et al. 1999).

Host galaxy	Source name	$\sigma_{\rm add}$ (″)	χ^2/ν
NGC 598 (M33)	X-8	2.2±0.1	22.6/16
NGC 891	SN 1986J	1.7±0.2	14.7/17
NGC 1313	Source A	1.3±0.2	13.9/14
	Source B	1.5±0.4	10.2/11
	SN 1978K	1.5±0.3	10.2/5
NGC 2403	Source 3	3.5±0.3	16.4/7
NGC 3031 (M81)	X-6	1.8±0.3	14.6/12
NGC 3628	off-center	1.8±0.5	9.9/4
NGC 6946	north-arm SNR	1.7±0.2	13.6/13
IC 342	Source 1	2.6±0.3	1.2/5
	Source 2	2.3±0.5	3.8/5

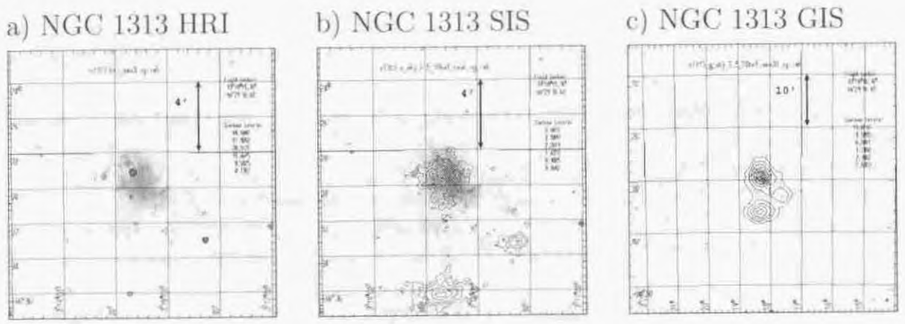

Figure 5.3: X-ray contours of NGC 1313, superposed on the optical (Digital Sky Survey) image. (a) The *ROSAT* HRI image. (b) The *ASCA* SIS image in the 0.5–10 keV band. (c) The *ASCA* GIS image in the same energy band as the SIS image. The HRI image, the SIS image, and the GIS image are smoothed with a gaussian distribution of $\sigma = 0.'05$, $0.'1$, and $0.'5$, respectively. All the images are displayed in sky coordinates using J2000 equinox, hence being rotated counterclockwise by $\sim 45°$ compared with Figure 5.1 and 5.2. Note that panel (c) has a different scale.

5.2 Light Curves of ULXs

As mentioned in the previous section, most of our sample objects can be regarded as point sources within the angular resolution of the *ROSAT* HRI ($\leq 10''$), and are likely to be single objects § 2.5.3. The source size can be limited more tightly when short-term variability is observed, since the size of the emission region should be less than the light speed multiplied by the the time scale of variability. Moreover, any spectral variation associated with time variability may provide us with a key information to identify the emission mechanism of ULXs. Therefore, we produced *ASCA* light curves of our ULXs (and also SNRs) to investigate their variability. The event extraction was performed over a circular region with a typical radius of $3'$. We use them also to accumulate the source spectra in Chapter 6, where details of the event accumulation region are described.

We added events from SIS 0 and SIS 1, or those of GIS 2 and GIS 3, and obtained SIS/GIS light curves in the 0.5–10 keV range, including background. We used only the SIS data for NGC 1365 SW-source and SNR in NGC 6946, to minimize the contamination from the neighboring sources, and only the GIS data for NGC 3628 off-center source, since the source drops in the SIS inter-chip gap. We did not utilize the data of M81 X-6 here, since the M81 nucleus located in the neighborhood is known to be variable (Ishisaki et al. 1996, Iyomoto 1999), which would affect the light curves of X-6.

We fitted the obtained light curves with a constant count rate model. The light curves are summarized in Appendix D, and the χ^2 values against the constant-intensity hypothesis are tabulated in Table 5.3. Thus, among the 33 light curves, three (IC 342 source 1 SIS/GIS and NGC 1313 source A in the 1995 observation SIS) show statistically significant ($\geq$99%) short-term variability, marginal (90–99%) variability is detected for another three (NGC 1313 source B in the 1993 observation SIS/GIS and IC 342 source 2

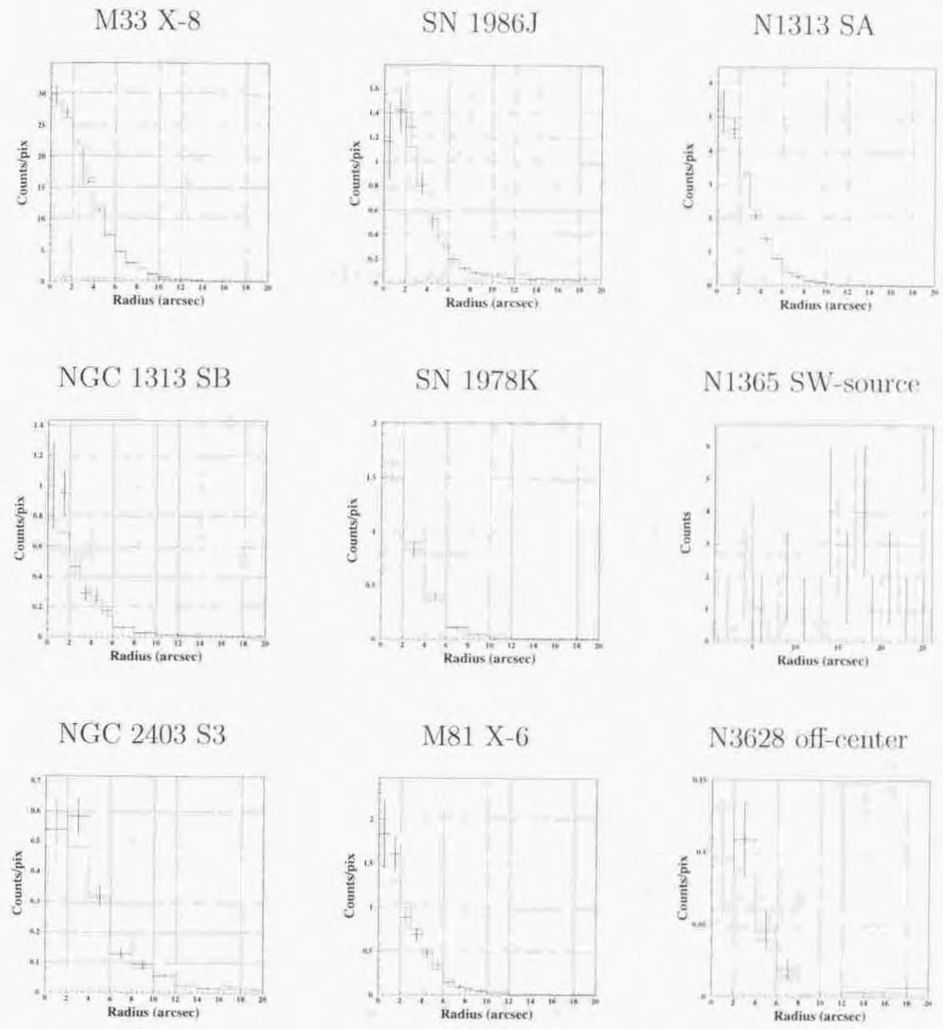

Figure 5.4: *ROSAT* HRI radial profiles of our sample objects, fitted with a modified PSF and a constant background (see text). The crosses represent the data, whereas the histograms indicate the model. For M33 X-8, a gaussian distribution is used instead of the constant background, and the contribution of each component is shown as dotted (modified PSF) and dot-dashed (gaussian distribution) lines. For NGC 1365 SW-source and two sources in NGC 4565, only the projected profiles are displayed.

NGC 4565

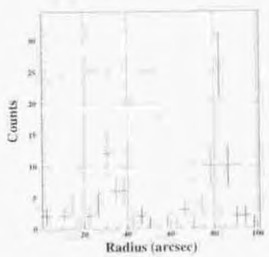

SNR in NGC 6946

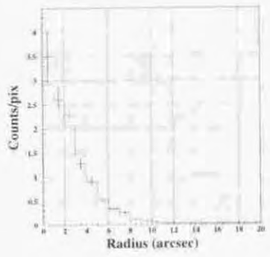

IC 342 S1

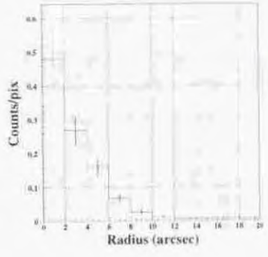

IC 342 S2

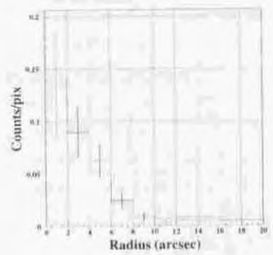

Figure 5.4: -*Continued.*

GIS), and the others are consistent with the constant count rate hypothesis. Here we show two fascinating cases in Figure 5.5, IC 342 source 1 andNGC 1313 source A in the 1995 observation, the former exhibited strong time variability as already reported by Okada et al. (1988), and the latter show intensity decreases. These two sources are highly unlikely to be composite objects. They are also difficult to be understood as a diffuse emission like SNRs, since the variability of 1–10 ks time scale limit their physical size within 10^{14}–10^{15} cm. For these two observations, we analyze the change of the spectral shape associated with the time variability in the next chapter. We also show the light curves of M33 in Figure 5.5, as an example of those which are consistent being constant.

Table 5.3: χ^2 values for ULX (and SNR) light curves against the constant-intensity hypothesis.

Host galaxy	Date	Source	Instrument	χ^2/ν
M33	99 07 22	X-8	SIS	45.0/50
	(position 1)		GIS	62.1/60
	99 07 23		SIS	36.3/37
	(position 2)		GIS	51.2/49
NGC 891	94 01 21	SN 1986J	SIS	40.2/34
			GIS	38.6/36
	96 01 29		SIS	40.3/45
			GIS	34.2/48
NGC 1313	93 07 12	Source A	SIS	46.6/45
			GIS	71.7/59
		Source B	SIS	56.1/37
			GIS	63.3/50
		SN 1978K	SIS	21.6/25
			GIS	33.6/34
	95 11 29	Source A	SIS	119.3/53
			GIS	66.1/53
		Source B	SIS	65.0/53
			GIS	56.8/53
		SN 1978K	SIS	28.4/28
			GIS	25.3/28
NGC 1365	95 01 25	SW source	SIS	21.5/27
NGC 2403	97 10 29	Source 3	SIS	52.9/44
			GIS	51.3/46
NGC 3628	93 12 12	off-center	GIS	18.8/22
NGC 4565	94 05 28	two ULXs are	SIS	45.3/43
		summed up	GIS	55.9/50
NGC 6946	94 12 28	North-arm SNR	SIS	38.5/45
IC 342	93 09 19	Source 1	SIS	321.6/60
			GIS	326.6/66
		Source 2	SIS	51.2/50
			GIS	79.3/62
Dwingeloo 1	95 09 14	X-1	SIS	60.9/63
			GIS	54.8/66

IC 342 Source 1 SIS

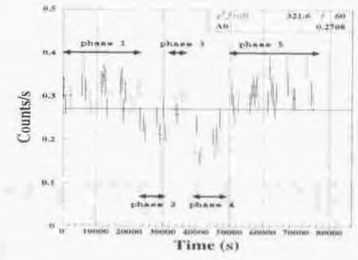

IC 342 Source 1 GIS

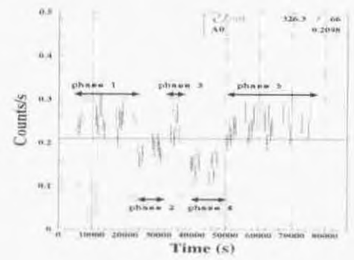

NGC 1313 source A SIS
in 1995

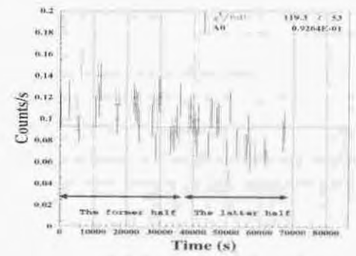

NGC 1313 Source A GIS
in 1995

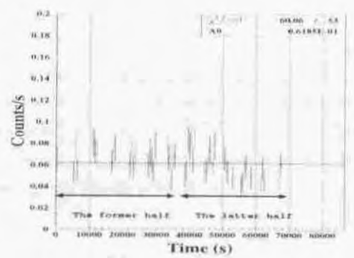

M33 SIS position1

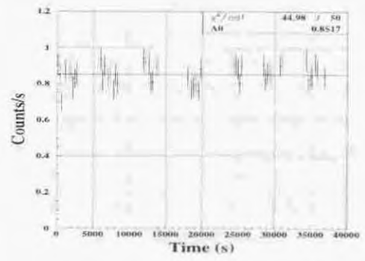

M33 GIS position1

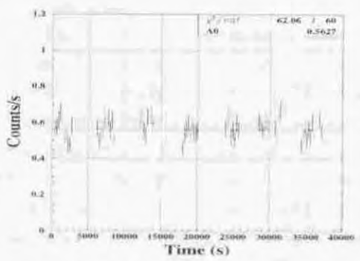

Figure 5.5: Examples of ULX light curves obtained by *ASCA* in the 0.5–10 keV energy range, including background. The typical background count rate is 0.02 and 0.01 c s^{-1} for the SIS and the GIS, respectively. Each light curve is tested against a constant-intensity hypothesis, and the assumed count rate is represented in the figure as a horizontal straight line. IC 342 source 1 and NGC 1313 source A (obtained in 1995 November) showed time variability, whereas the light curves of M33 are consistent with being constant. The light curves of the other sources are summarized in Appendix D.

Chapter 6

SPECTRAL PROPERTIES OF ULXs

6.1 Spectral Analysis

Spectra of ULXs will provide us with a key information on the source nature. Since *ASCA* has a wide effective area over a wide energy band (0.5–10 keV) together with the improved energy resolution, we can obtain high-quality spectra of ULXs which have not been provided by any previous missions. Before describing the individual spectra of ULXs, we briefly explain the procedure of spectral analysis in this section.

6.1.1 Accumulation of source and background spectra

As mentioned in § 3.2, the *ASCA* XRT has rather poor spatial resolution; half power diameter is $\sim 3'$ (Table 3.1), and its point-spread function exhibits broad wings that extend beyond $\sim 10'$. Therefore, we have to use relatively wide integration regions, typically $\sim 3'$ in radius, to accumulate the source spectrum, even for point sources. The on-source spectrum accumulated in this way includes not only signal photons from the target source, bus also background events (§ 3.5) that must be estimated separately and then subtracted away. For the GIS, the background spectrum is obtained from blank-sky data, by accumulating events within the same region as is used for extracting the source spectrum. For the SIS, on the other hand, the background spectrum is obtained in most cases from source-free regions of the same observation. This is because the non X-ray background of the SIS detector depends on the SIS clocking mode, and has gradually changed since the launch of *ASCA* due to radiation damage (§ 3.3.3 and § 3.5). However, for a limited number of observations performed in a 4-CCD mode in early phases of the mission (roughly speaking, within one year since the launch), we can derive the SIS background spectrum from blank-sky data, that were also taken in the 4-CCD mode. This improves the photon statistics, since we can sum up many blank-sky data to achieve a long exposure, e.g. $\geq$100 ks in total. When the source is located on the Galactic plane, such as Dwingeloo 1 X-1 (§ 4.2), we use source free regions of the on-source data to obtain the background spectrum for both the SIS and the GIS, in order to eliminate diffuse emission from the Galactic plane, called Galactic Ridge X-ray Emission (Worral et al. 1982, Koyama et al. 1986, Kaneda 1998). We quantify the background-subtracted spectrum in terms of various spectral models, either theoretical or empirical, as described in the next

subsection.

6.1.2 Detector response and spectral fitting

We usually quantify the background-subtracted spectrum in the following way; first modeling the spectrum, then multiplying it with the instrumental response, and finally comparing the model-predicted pulse-height distribution with the actually observed spectrum. More specifically, expected pulse-height distribution $S(PHA)$ is calculated from the model function $M(E)$ as

$$S(PHA) = \sum_E R(PHA, E) A(E) M(E) \quad ,$$

where E is the X-ray energy, PHA is the observed pulse height, $A(E)$ is called ancillary response file (ARF), and $R(PHA, E)$ is called response matrix file (RMF). Simply saying, the ARF is an instrumental efficiency as a function of incident X-ray energy and expressed in the form of a vector, whereas the RMF describes the expected pulse-height distribution for incident monochromatic X-rays of energy E and expressed in the form of a matrix. The ARF is contributed by both the XRT and the detector (the SIS or the GIS), while the RMF is determined by the detector alone.

In order to extract the spectrum, we must specify the position, shape (mostly circular centered on the source) and size of the extracting region. The ARF depends on the size and position of the extracting region, so that we should calculate ARF for each observation. On the other hand, the RMF is thought to be the same over the whole detector area of the GIS, and we can use the standard single RMF. Since the detector response of the SIS shows time variability due to radiation damage (§ 3.3.3), we calculate the SIS RMF for each observation.

Although the response ($ARF \times RMF$) is not the same among the four sensors (SIS 0, SIS 1, GIS 2, and GIS 3), the difference between the two SISs or the two GISs is relatively small. Therefore, we sum the two SIS (SIS 0 and SIS 1) spectra into a single SIS spectrum, and the two GIS (GIS 2 and GIS 3) spectra into a single GIS spectrum, in order to improve photon statistics when analyzing the spectra of ULXs. We also sum the detector response ($ARF \times RMF$) in the same way. Thus, we obtain the spectrum and detector response for the SIS and the GIS, and fit them jointly. We use the χ^2 minimization method to find the best fit parameters. That is, we adopt a single spectral model, calculate model predictions for the SIS and the GIS using respective responses, compare the predictions to the corresponding spectra, and sum up the χ^2 values from the two instruments. Unless otherwize stated, we estimate errors of one interesting parameter as 90% confidence range, i.e., the value of χ^2 is decreased by 2.71 from the minimum value.

Before performing actual spectral fittings of ULXs, we must examine how the response and model uncertainties affect the obtained results. As mentioned in Appendix B, the GIS (plus XRT) spectral response at the nominal focal-plane position has been calibrated (except the flux normalization) down to an uncertainty of ~1.5%, which is small enough compared with the photon statistics of our sources. Therefore for the GIS data, we consider only the statistical errors in calculating the χ^2 values. For the SIS, the spectral response is cross-calibrated with the GIS by observing moderately strong sources, e.g., 3C273, which is more than 10 times brighter than any of our sample objects. Hence, we assume the calibration uncertainty of the SIS to be at a comparable level to that of the GIS, and calculate the values of χ^2 based on the statistical errors alone, too. The effect

of these response uncertainties on the spectral results is described in § 6.2.1 and § 6.3.2, for ULXs having relatively good photon statistics

We should also consider how the spectral results depend on the source position on the focal plane. As for the spectral shape, Fukazawa et al. (1997) confirmed that the dependence on the source location is relatively small based on the multi-pointing observations of the Crab Nebula; the derived photon index Γ scatters $\sim \pm 0.05$ over a major part of the GIS field of view (see Appendix B). This implies $\sim \pm 12\%$ difference in the flux ratio at 1 keV to 10 keV. If we assume an MCD spectrum (see § 2.7) of $T_{\rm in} = 1.5$ keV, this difference corresponds to only $\pm 2\%$ uncertainty in the value of $T_{\rm in}$. As shown in later part of this chapter, this uncertainty is much smaller than the statistical errors for all of our sample ULXs, hence negligible. On the other hand, Fukazawa et al. (1997) reported that the measured flux depends by $\sim \pm 10\%$ on the observed position, as also described in Appendix B. Actually, we often find that the SIS and the GIS spectra require somewhat discrepant model normalizations by up to $\sim 15\%$, particularly depending on the source location on the focal plane. Accordingly, in the joint spectral fitting, we require the model to have identical shapes between the SIS and the GIS, but allow the relative normalization to be free between them. As a result, the two instruments sometimes give slightly different source fluxes. In such a case we generally refer to the GIS flux, because the SIS results sometimes suffer from the inter-chip gaps. The flux uncertainty by 10–20% does not affect our discussions in Chapter 7. We emphasize that the SIS/GIS discrepancy occurs only in their relative photometric normalization, not in the spectral shape.

We finally examin the influence of utilizing an MCD approximation instead of a standard Shakura & Sunyaev model (see § 2.7 for model descriptions). For this purpose, we numerically calculated spectra expected from a standard disk model, with the peak temperature of 1.0, 1.5, and 2.0 keV. They are modified with photoelectric absorption (see Appendix A) of $N_{\rm H} = 0.1 \times 10^{22}$ cm^{-2}, and convolved with the *ASCA* spectral response function to produce simulated spectral datasets. Then, we fitted the obtained spectra with an absorbed MCD model. Regardless of the assumed peak temperature, the fit residuals are at most $\sim 7\%$, and only $\leq 2\%$ in the energy range of 0.7–7 keV, implying that the difference between these two models is almost indistinguishable, as shown in Figure 6.1. Although the obtained values of $N_{\rm H}$ (0.07–0.09 $\times 10^{22}$ cm^{-2}) are somewhat smaller than what was assumed initially, the difference is again smaller than the statistical errors of our sample objects. Therefore, the MCD approximation does not affect our spectral analysis, either.

6.2 IC 342 Source 1

Among our sample, IC 342 source 1 has the highest flux next to M33 X-8, and one of the highest luminosities up to $L_{\rm X} \sim 10^{40}$erg s^{-1}, as shown in Table 2.2. Therefore this source can be regarded as a typical ULX, and is suitable for the start point of our spectral studies. As shown in Figure 5.5, this source showed strong time variability during the *ASCA* observation, while the spectral shape also changed as reported by Okada et al. (1998). We first study the time-averaged spectra in § 6.2.1–§ 6.2.3, and then sort the data in § 6.2.4 according to the source intensity and study the spectra individually.

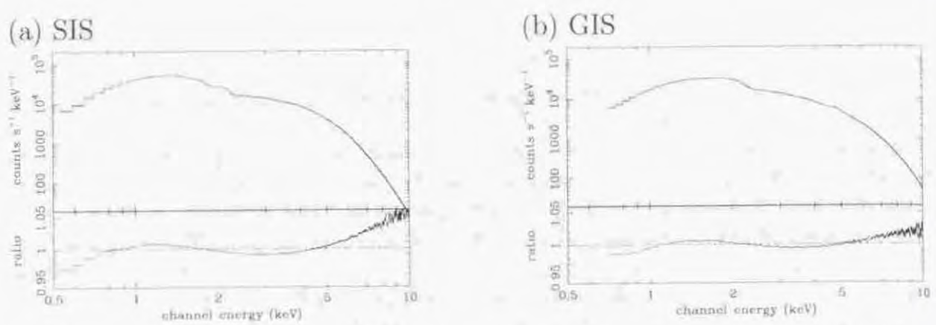

Figure 6.1: The SIS/GIS simulated spectra expected from a Shakura & Sunyaev disk with the peak temperature of 1.5 keV and $N_{\rm H} = 0.1 \times 10^{21}$ cm^{-2}, convolved with the corresponding detector response. They are fitted with an absorbed MCD model, and the data-to-model ratios are shown in the lower panels.

6.2.1 Time averaged spectrum

We extracted the SIS and GIS spectra from a circular region of 3′ radius centered on the source. The size of the region is determined to avoid the overlap with the region used to extract the spectrum of source 2 (§ 6.8), and is the same as that utilized previously by Okada et al (1998). The background spectra were obtained from blank-sky data, and were subtracted from the source spectra. Before performing spectral fitting, we plotted the "unfolded" (detector efficiency removed) spectra in Figure 6.2. Although unsuitable for quantitative analysis, the unfolded spectra are useful to visualize rough spectral properties. In fact, the counts in the low-energy range ($\leq$1.5 keV) drop off, implying that the actual spectra suffer absorption. In addition, the continua exhibits a rather convex curvature. These features are confirmed by the spectral fitting as performed below.

We fitted the background-subtracted spectra with typical single component models; a power-law model, a thermal Bremsstrahlung (TBS) model, a Raymond-Smith (R-S) plasma emission model, or a multi-color disk blackbody (MCD) model, each multiplied by the factor representing photoelectric absorption due to an interviewing gas with an equivalent hydrogen column density of $N_{\rm H}$. A power-law model is one of the simplest, widely used model, and also represents non-thermal emission as is seen from AGNs, X-ray pulsars, and so on. This model is characterized by a photon index Γ. A TBS model is a thermal emission from optically-thin plasmas and characterized by its temperature. This model also approximates the spectrum from bright LMXBs (§ 2.3.2). A R-S model describes thin-thermal emission with lines emitted by hot plasmas, of which the metal abundance and the plasma temperature are the characteristic model parameters. An MCD model (see § 2.7) represents emission from optically-thick accretion disks around NSs or BHs. The inner-most disk temperature, $T_{\rm in}$, determines the spectral shape, whereas the inner-most disk radius, $R_{\rm in}$, determines the normalization. Further details of these models are described in Appendix A.

The results of the spectral fitting with these models are summarized in Table 6.1 and

Figure 6.3. Thus, the single power-law model is completely unacceptable. The R-S model requires quite low metallicity, so that it is almost identical to the TBS model: this is the reason why we do not show the Raymond-Smith fit in Figure 6.3. In any case, the R-S and TBS fits are also rejected with a high significance (at 99% confidence). The fit residuals of these models in Figure 6.3 imply that the actual spectrum has rather convex shape in logalithmic plot, in agreement with the impression of Figure 6.2. In fact, the MCD model, which has the most convex shape among our four models tested here, can successfully represent the data. The value of $N_{\rm H}$ obtained with the MCD model is not much different from the Galactic line-of sight column density (3×10^{21} cm^{-2}). In contrast, the other unsuccessful models require larger values of $N_{\rm H}$, in order to make the model shape artificially more convex than it is.

As already described in § 2.7.1 and § 6.1.2, the MCD model is almost indistinguishable from the standard Shalura & Sunyaev one. Actually, the fit is not improved significantly by replacing the MCD model with the standard model; the value of χ^2 has decreased only by 0.5, implying that the MCD approximation does not affect the confidence level. We also considered the influence of the detector response uncertainty on the value of χ^2. As we have seen in the previous section, the calibration uncertainty of the response functions is estimated to be $\sim$ 1.5%. Thus, we introduced 1.5% systematic errors on the spectral fitting of this ULX (fitted with the single MCD model). Then, the decrease of the χ^2 value is only 4.4, which do not affect our statement of the model acceptability either.

6.2.2 Limits on the hard component

Thus, the spectra of IC 342 source 1 can be reproduced successfully with the MCD model, which describes optically thick emission from a standard accretion disk around a compact object (§ 2.7 and Appendix A). So far, the MCD spectra have been observed from two types of Galactic XRBs; one is LMXBs, and the other is BHBs in the soft state (§ 2.3.2 and § 2.3.4). In addition to the MCD component, Galactic LMXBs generally exhibit a black-body component of kT $\sim$2 keV, and Galactic BHBs in the soft state often show a hard component that can be expressed with a power-law of photon index Γ=2.0–2.5. Therefore, we investigate the presence of these hard components in the spectra of IC 342 source 1.

We refitted the spectra by adding a black-body component or a power-law component to the MCD model. We fixed the temperature of the black-body component at 2 keV, a typical value observed from LMXBs, in order to obtain a stable fitting. We also fixed the photon index of the power-law component at 2.2, to simulate typical spectra of BHBs in the soft state. However, the data did not require either hard component. The reduction of χ^2 is only 0.7 by including the power-law component, and 2.2 by including the black-body component. Therefore, the presence of these hard components is insignificant at 90% confidence from an F-test. The contribution to the 0.5–10 keV flux of the power-law component is only $\sim$20% at most (at 90% confidence), and the best-fit MCD temperature, $T_{\rm in}$, increased slightly to 1.81 keV. This value is the same, within the statistical errors, as obtained when we fit the spectra with the MCD model alone. The contribution of the black-body component to the flux in the same energy range is also low, $\sim$30% at most, although the best-fit value of $T_{\rm in}$ decreased noticeably to 1.33 keV.

6.2.3 Other acceptable models

Although the single MCD model successfully represents the spectrum of IC 342 source 1, there remains a possibility that other single component models can also express the spectrum adequately. The source is suitable for such a study, because of its high photon statistics.

Any model to be tested here must have a mildly convex shape, like the MCD model. One possibility is so-called unsaturated Comptonization (UC) model, expected when hot thermal electrons Compton up-scatter some soft seed photons into X-rays. This model is characterized by an electron temperature, T_e, and an optical depth for electron scattering, τ_{es}. Another popular empirical model having an MCD-like shape is a broken power-law model, which is frequently used to represent synchrotron emission, e.g., from blazars. This model is characterized by three parameters; photon indices in the lower and higher energies, Γ_1 and Γ_2 respectively, and the break-point energy, E_{bk}. Further details of these two models are described in Appendix A.

We jointly fitted the GIS and SIS spectra with these two models, and summarize the results also in Table 6.1 and Figure 6.3. Thus, the broken power-law fit is somewhat poor: it is rejected at 90% confidence. Although the UC model is statistically acceptable, it shows a relatively worse χ^2 compared with the MCD model, or, in other words, the confidence level is lower than that of the MCD one (25% for the UC model whereas 43% for the MCD one). We furhter examined whether the response uncertainty of 1.5% affects this choice of the best-prefereed model. For this purpose, we introduced the uncertainty in a conservative manner, i.e., we artificially increased the observed source counts by 1.5% at 10 keV, reduced by 1.5% at 0.5 keV, and modified for the intermediate enery based on the linear interpolation (or, vise versa). Then we re-fitted the obtained spectra with the MCD, the UC, and the broken power-law model, and found that the change of the χ^2 value is below 0.5. Thus the MCD model is certainly preferred than the other two models with respect to the fit confidence. In addition, both the UC and broken power-law models require excess absorption compared with the MCD one. We discuss physical meanings of them in Chapter 7. In summary, the single MCD model gives the best description of the observed spectra of IC 342 source 1. We therefore use this model as a standard tool to analyze the spectra of other objects among our sample.

6.2.4 Time variability

Now that we have quantified the average spectrum of IC 342 source 1, we examine its time variability. We hence divided the data into five time regions, as defined in Figure 5.5. In order to grasp the rough spectral information, we first summed phase 2 spectra and phase 4 spectra into "low-flux phase" spectra, and summed phase 1, 3, and 5 spectra into "high-flux phase" spectra, and fitted them with an MCD model, which successfully reproduce the time-averaged spectrum. Then, as summarized in Table 6.2 and Figure 6.4, the MCD model again turned out to be successful, and provide the value of absorption consistent with the time-averaged one. Therefore we fitted five time-sorted spectra by the MCD model, with the absorption fixed at the best-fit value of time-averaged spectra, i.e., N_H=4.7×10^{21} cm^{-2}. The results are summarized in Table 6.3. Thus, all the five spectra are well fitted and an positive correlation between T_{in} and f_X is clearly seen.

As described in § 2.7, the MCD model provides us with two basic quantities of the

accretion disk; the inner-most disk temperature, T_{in}, and the inner-most disk radius, R_{in}. In order to examine changes in these two quantities, we plotted the confidence contours of the five spectra on the T_{in}–R_{in}^2 plane in Figure 6.5. Thus, R_{in} gradually decreases as T_{in} increases, and the relation is approximated as $R_{in} \propto T_{in}^{-1}$. Further examination of these results will be performed in Chapter 7.

Table 6.1: Joint fit results of the SIS/GIS spectra of IC 342 source 1 using single component models.

Model	N_H (10^{22}cm^{-2})	Parameters[a]	f_X [b] (0.5–10 keV)	χ^2/ν (confidence level)
Power-law	0.93±0.06	1.90±0.05	11.1	266.5/135 (≤1%)
TBS	0.75±0.04	6.7±0.6	10.7	183.2/135 (≤1%)
R-S[c]	0.75±0.04	6.8±0.5	10.7	183.7/134 (≤1%)
MCD	0.47±0.03	1.77±0.05	10.2	137.4/135 (43%)
UC	0.64±0.07	1.42±0.09/23±2	10.2	144.9/134 (25%)
Broken power-law	$0.63^{+0.10}_{-0.07}$	$1.39^{+0.18}_{-0.13}/2.38^{+0.40}_{-0.15}/3.6^{+0.7}_{-0.4}$	10.7	156.3/133 (8%)

[a] Photon index for the power-law model, plasma temperature (keV) for the TBS and R-S model, T_{in} for the MCD model, T_e (keV)/τ_{es} for the UC model, and $\Gamma_1/\Gamma_2/E_{bk}$ (keV) for the broken power-law model.
[b] In unit of 10^{-12} erg s^{-1} cm^{-2}.
[c] The abundance has been constrained to be ≤0.03 solar.

Table 6.2: Time variability of IC 342 source 1. The SIS/GIS spectra of the high and low flux phases are fitted with a single MCD model.

Phase	N_H (10^{22}cm^{-2})	T_{in} (keV)	f_X [a] (0.5–10 keV)	χ^2/ν (confidence level)
High-flux	0.47±0.04	1.87±0.07	11.6	129.0/106 (6%)
Low-flux	0.47±0.07	1.42±0.09	6.4	115.6/107 (27%)

[a] In unit of 10^{-12} erg s^{-1} cm^{-2}.

6.3 M33 X-8

The *ASCA* spectra of M33 X-8 have been interpreted by Takano et al. (1994) as emission from an accreting BH of ∼10$M_\odot$, as mentioned in § 2.6. We here attempt to reconfirm their results, using the instrumental responses which have been updated significantly since Takano et al. (1994) was published.

6.3.1 Single component fits

M33 was observed with *ASCA* twice in July 1993, as tabulated in Table 4.1. Since the two observations were performed in series, and the source intensity did not change between the two occasions, we co-add data from the two observations. We accumulated the source spectra over circular regions centered on the source, with radii of 4′ and 6′ for the SIS

Table 6.3: Fitting results of time-sorted spectra of IC 342 source 1. The SIS/GIS spectra are fitted jointly with the MCD model, fixing absorption at $N_{\rm H}$=4.7×10^{21}cm^{-2}.

Phase	$T_{\rm in}$ (keV)	$f_{\rm X}$ [a] (0.5–10 keV)	χ^2/ν (confidence level)
1	1.96±0.10	12.2	59.2/81 (97%)
2	1.50±0.10	7.5	60.4/63 (57%)
3	1.70±0.15	9.6	52.2/48 (31%)
4	1.29±0.08	5.5	54.3/60 (68%)
5	1.81±0.07	11.3	136.9/117 (10%)

[a] In unit of 10^{-12} erg s^{-1} cm^{-2}.

(a) Unfolded spectrum, SIS

(b) Unfolded spectrum, GIS

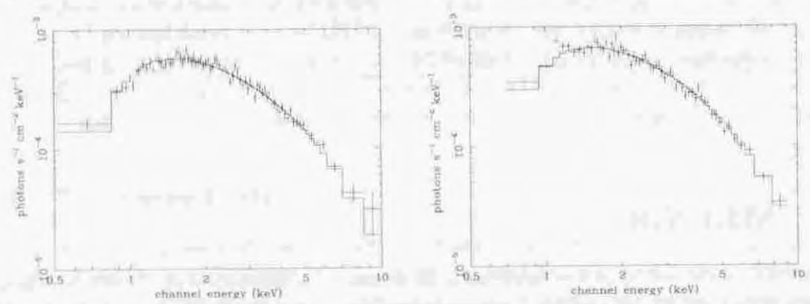

Figure 6.2: The background-subtracted, unfolded SIS and GIS spectra of IC 342 source 1, where the crosses represent the observed spectra. For comparison, we also plotted the best-fit MCD model (see Table 6.1) as histograms.

(a) Power-law

(b) TBS

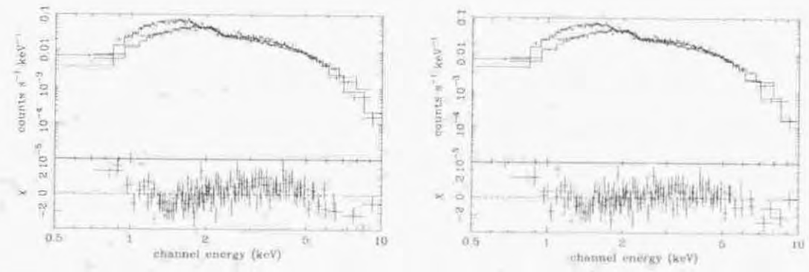

(c) MCD

(d) UC

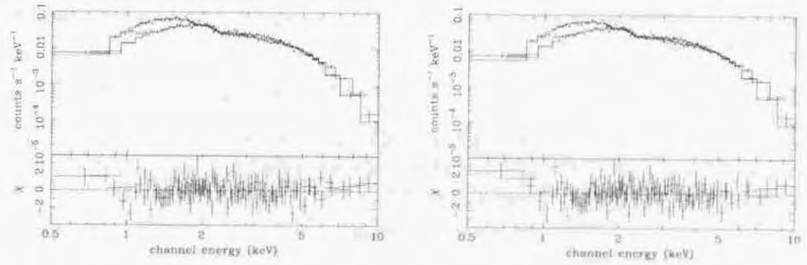

(e) Broken power-law

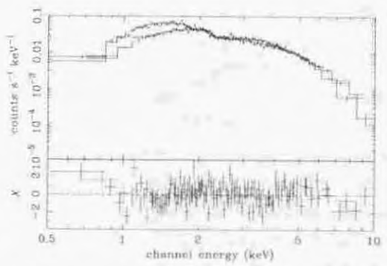

Figure 6.3: The background-subtracted SIS and GIS spectra of IC 342 source 1, fitted jointly with various single-component models with photoelectric absorption. The histograms show the best fit model and the crosses represent the observed spectra. The lower panel shows the fit residuals. The SIS data shows higher counts in lower energies, whereas the GIS shows higher counts in higher energies. The employed models are a power-law, a TBS, an MCD, a UC, and a broken power-law model. We do not show the R-S model fit, since it is almost identical to the TBS model.

(a) High flux phase

(b) Low flux phase

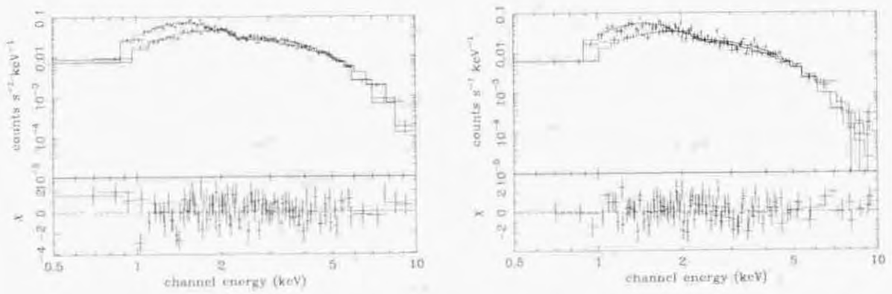

Figure 6.4: The background-subtracted SIS and GIS spectra of IC 342 source 1. Panel (a) represents the spectra obtained at the high-flux phase, whereas panel (b) the low-flux one. Both are fitted jointly with the MCD model.

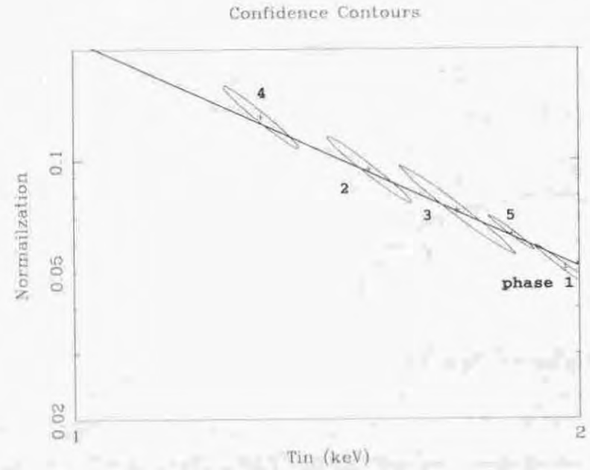

Figure 6.5: The confidence contours of the MCD fit in terms of $T_{\rm in}$ and the normalization of the MCD model, which is proportional to $R_{\rm in}^2$. The confidence level of 68% is shown. We fixed the absorption at $N_{\rm H}$=4.7×10^{21}cm^{-2}. The solid line represents the relation of $T_{\rm in} \propto R_{\rm in}^{-1}$. The horizontal axis is logalithmic.

and the GIS, respectively, and subtracted the background spectra derived from blank-sky observations. The obtained spectra were then fitted with the typical single component models that we used for IC 342 source 1 in the previous section; a power-law, a TBS, a R-S, or an MCD model, each multiplied by photoelectric absorption. In this particular case, however, the SIS and GIS data showed some discrepancy in the lower energy range below $\sim$ 1 keV, presumably because of calibration uncertainties in the soft X-ray range. This is known to occur occasionally with the *ASCA* data, particularly when the source has high signal statistics like in the present case. To cope with this problem, we allowed the values of $N_{\rm H}$ to be different between the SIS and the GIS.

As presented in Table 6.4 and Figure 6.6, the power-law model failed completely, and the MCD model was also unacceptable at 99% confidence level. In contrast, the TBS and R-S models are both successful. (They are essentially the same, because the R-S fit requires a quite low metallicity.) Thus, the M33 X-8 spectra on average exhibit a mildly convex shape, which can be represented by a TBS model of $kT = 3$ keV. A power-law model is too straight, while an MCD model is too convex. The discrepancy in $N_{\rm H}$ between the two instruments turned out to be $(0.05 - 0.1) \times 10^{21}$ cm^{-2}, which is small enough for our purpose.

6.3.2 Double component fits

Although the single MCD model thus failed to reproduce the X-8 spectra, we need to investigate the cause of the failure more closely, because the MCD model has already given the best description to the spectra of IC 342 source 1, a typical ULX. Actually, in Figure 6.6c, the residuals are significant only in energies above $\sim$ 5 keV. This suggests that the failure is caused by the presence of a separate hard component, rather than by a discrepant continuum curvature.

Accordingly, we proceed to fit the M33 X-8 spectra with double-component models consisting of an MCD emission and a hard tail, as we have performed on IC 342 source 1 in § 6.2.2. As the hard component, we again use either a power-law with photon index fixed at $\Gamma = 2.2$, or a blackbody with temperature fixed at $kT = 2.0$ keV. Then, either modeling has given a fully acceptable joint fit to the data, as summarized in Table 6.5 and Figure 6.7. The fit χ^2 has decreased by 84.4 and 78.6 for the power-law and blackbody modeling, respectively. Therefore, the hard component is statistically quite significant. The achieved values of χ^2 are also significantly lower than that from the single TBS fit. We thus consider that the spectrum of M33 X-8 can be better described by an MCD plus hard-tail model than by a single TBS one.

Comparing the two modelings of the hard-tail in Table 6.5, the power-law modeling gives a lower value of χ^2 than the blackbody one. Furthermore, a power-law hard tail is often observed to accompany the MCD emission from BHBs (§ 6.2.2). Therefore, we regard the MCD component with a power-law hard tail as the best representation of the M33 X-8 spectrum. We thus reconfirm the conclusion reached by Takano et al. (1994). In this modeling, our best-fit MCD temperature, $T_{\rm in} = 1.15 \pm 0.03$ keV, is somewhat higher than those obtained by Takano et al. (1994); $T_{\rm in} = 0.98 \pm 0.06$ keV from the SIS, and $T_{\rm in} = 1.06 \pm 0.06$ keV from the GIS. This is partly because we fixed the index of the power-law component at Γ=2.2, whereas they fixed at Γ=1.8. If we fixed the index at 1.8, we again obtain an acceptable fit (χ^2/ν=169.6/199) and $T_{\rm in}$ decreases to 1.09±0.03 keV. The residual difference between our value of $T_{\rm in}$ and that of Takano et al. (1994) is

thought to reflect the progress in the instrumental calibration.

Like IC 342 source 1, we investigated the influence of the model and response uncertainties on the fit acceptance, and obtained the same results; the value of χ^2 has not changed for the MCD plus power-law fit by replacing the MCD model with the standard Shakura & Sunyaev one, and decreased only 9.0 by inclusion of the 1.5% response uncertainties. The modification of the observed source counts by $\pm 1.5\%$ changed the χ^2 values by only ≤ 0.5 for the MCD plus power-law or the MCD plus black-body model fitting. Thus, statements of the model acceptance are not affected.

Table 6.4: Joint-fit results of the M33 X-8 spectra, using single component models.

Model	$N_{\rm H}$ [a] (10^{22}cm^{-2})	Γ or kT or $T_{\rm in}$ (keV)	$f_{\rm X}$ [b] (0.5–10 keV)	χ^2/ν (confidence level)
power-law	0.41/0.37	2.34	20.1	569.6/201 ($\leq$1%)
TBS	0.22±0.01/0.15±0.03	3.4±0.1	19.6	211.2/201 (30%)
R-S[c]	0.22±0.01/0.15±0.03	3.4±0.1	19.7	213.5/201 (24%)
MCD	0.06±0.01/$\leq$0.01	1.18±0.02	19.1	251.6/201 ($\leq$1%)

[a] SIS/GIS.
[b] In unit of 10^{-12} erg s^{-1} cm^{-2}.
[c] The abundance has been constrained to be $\leq$0.01 solar.

Table 6.5: Joint-fit results of the M33 X-8 spectra, using the MCD model with a hard component.

Model[a]	$N_{\rm H}$ [b] (10^{22}cm^{-2})	$T_{\rm in}$ (keV)	$f_{\rm X}$ [c] (0.5–10 keV)	χ^2/ν (confidence level)
MCD+power-law	0.18±0.02/0.09±0.04	1.15±0.03	19.8	167.2/200 (94%)
MCD+black-body	0.08±0.01/$\leq$0.01	1.03±0.03	20.0	173.0/200 (92%)

[a] The power-law index is fixed at Γ=2.2, and the temperature of the black-body at kT=2.0 keV.
[b] SIS/GIS.
[c] In unit of 10^{-12} erg s^{-1} cm^{-2}.

6.4 M81 X-6

Aw we have shown in Table 2.1 in § 2.5.1, M81 hosts a ULX, called X-6 (Fabbiano 1988). Since M81 has a Cepheid-based accurate distance of 3.6 Mpc (Freedman et al. 1994), we can calculate the luminosity of X-6 without being affected by the distance uncertainty. Moreover, *ASCA* has observed this galaxy more than 10 times in order to study the newly exploded supernova, SN 1993J (Kohmura 1994, Uno 1997). This fact enables us to study the long-term variability of X-6. In this thesis we use data obtained after 1994, in

(a) Power-law

(b) TBS

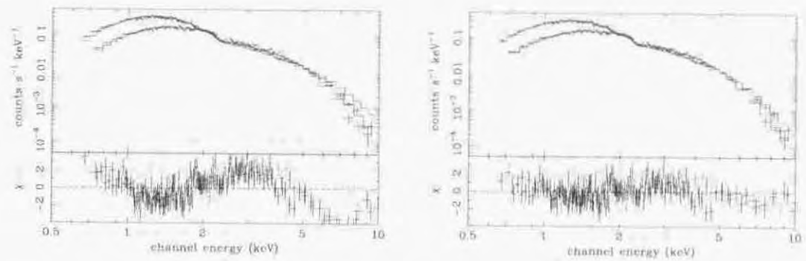

(c) MCD

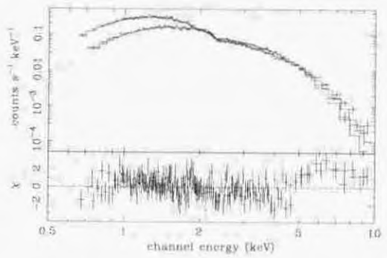

Figure 6.6: The background-subtracted SIS and GIS spectra of M33 X-8, jointly fitted with single component models; a power-law, a TBS, and an MCD model. The R-S model fit is almost identical to the TBS fit.

(a) MCD+power-law, SIS

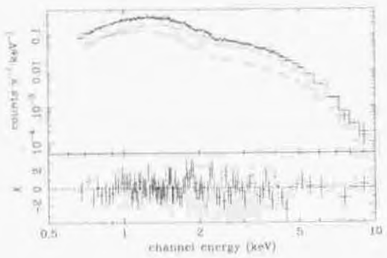

(b) MCD+power-law, GIS

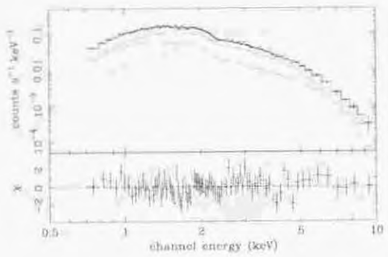

(c) MCD+black-body, SIS

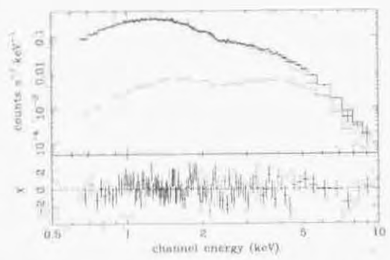

(d) MCD+black-body, GIS

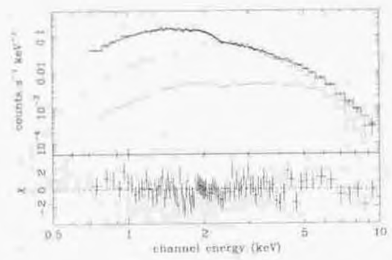

Figure 6.7: The background-subtracted M33 X-8 spectra of the SIS and GIS, fitted with double-component models. The contributions of the two components are shown by dotted lines. Although the fit is simultaneous to the SIS and GIS, we show the two spectra separately for clarify.

which SN 1993J had faded away significantly and its contamination to the X-6 spectrum is sufficiently low, as described below. Thus we analyzed seven observations in total, as shown in Table 4.1. The same datasets were already utilized by Uno (1997) in his study of SN 1993J.

6.4.1 Accumulation of the source and background spectra

When studying the spectrum of X-6, we should eliminate contamination from the two nearby sources, SN 1993J and M81 X-5, the latter begin the LLAGN of M81 (Ishisaki et al. 1996, Iyomoto 1999). As shown in Figure 6.8, X-6 is separated only $\sim 1'$ from SN 1993J, and $\sim 3'$ from X-5.

We accumulated the source spectrum of X-6 from a circular region of 1.'5 radius, which is significantly smaller than those for other sources, since a larger area would make the X-5 contamination serious. We only used the SIS data, since the poorer spatial resolution of the GIS increases the X-5 contamination. In the obtained spectrum, however, typically $\sim$50% photons still originate from X-5 because of its brightness. In order to remove this residual contamination, we accumulated a background spectrum over another region having the same size as was used for the on-source spectrum. This background region is located opposite to X-6 with respect to X-5, as shown in Figure 6.8, where we expect a similar amount of contamination from X-5. We multiplied a constant factor to thus obtained background spectrum, then subtracted it from the source spectrum. This "scaling factor" is introduced to take into account the *ASCA* XRT's asymmetric PSF (§ 3.2.2), and is determined based on the ray-tracing (Monte-Carlo) simulation, developed by the XRT team. By simulating the X-5 event for each observation (each position of X-5 on the focal plane), we can estimate the ratio of photons in the source region to the background region. The ratio, or the scaling factor, is typically 1.5, ranging over 1.2–1.8.

Thus, we have obtained the spectrum for X-6 plus SN 1993J. The contamination from SN 1993J is difficult to eliminate because of their short separation. Instead, we take it into account in a different way. The SN 1993J spectrum was separately estimated by Uno (1997) through one-dimensional SIS image analysis, which was originally developed by Kohmura (1994). According to Uno (1997), SN 1993J had faded away significantly after one year from the explosion, and the spectrum is expressed by a power-law of Γ=2.5 and $f_{\rm X} = 0.5 \pm 0.2 \times 10^{-12}$ erg s^{-1} cm^{-2} in 1994 April, and of Γ=3.0 and $f_{\rm X} = 0.2 \pm 0.1 \times 10^{-12}$ erg s^{-1} cm^{-2} in 1994 October, both in the 0.5–8 keV band. We calculate their contamination to our spectrum based on the ray-tracing simulation, and take the results into account as a fixed power-law function when fitting the X-6 spectrum. The contribution of SN 1993J to the 0.5–10 keV flux turned out to be $\sim$ 10% and $\sim$ 3% in 1994 April and October, respectively. For the other data which were obtained after 1995 April, we neglect the contribution from SN 1993J, since the supernova further faded away.

6.4.2 Spectra of individual observations

We fitted the obtained seven spectra separately with our typical single component models, and summarized the results in Table 6.6 and Figure 6.9. Thus, the MCD model generally provides the lowest values of χ^2. Moreover, the other models are sometimes rejected at 90% confidence level, whereas the MCD fit is always acceptable. Therefore we conclude

that the spectra of M81 X-6, like those of IC 342 source 1, can be represented well by the single MCD model.

As was done on IC 342 source 1, we make the $T_{\rm in}$–$R_{\rm in}^2$ diagram and show it in Figure 6.11a. It indicates that our seven datasets can be grossly grouped into two representative state; a low-temperature state observed in 1995 October and 1996 April, and a high-temperature state observed on the other occasions. The low/high-temperature states correspond to the low/high-flux states; thus M81 X-6 shows similar spectral variability to IC 342 source 1. However we do not necessarily mean that the variation of X-6 is bimodal.

6.4.3 Spectrum of two states

According to Figure 6.11a, we summed up the seven spectra into two spectra; the high-temperature state spectrum, and the low-temperature state one. We fitted these two spectra by the same single component models as we used on IC 342 source 1, and obtained results as summarized in Table 6.7 and Figure 6.10. The power-law model has completely failed, and the TBS and R-S models are also highly unacceptable at 95% confidence. The other three models can equally represent the data, although the broken power-law model shows slightly smaller χ^2/ν.

We also included a hard component to the MCD fit; a power-law component of Γ=2.2 or a black-body component of kT=2.0 keV. Again, the presence of these hard components turned out to be insignificant, and the contribution to the 0.5–10 keV flux of the hard components is small; only ∼20% at most (90% confidence) when using the black-body modeling in the low-temperature state spectrum, and ∼30% for other combinations.

We finally plotted the confidence contours of the two subgrouped spectra on the $T_{\rm in}$–$R_{\rm in}^2$ plane, by fixing the absorption at the average value of the two states, $N_{\rm H}$=1.8×10^{21}cm^{-2}. As shown in Figure 6.11b, $R_{\rm in}$ increases marginally as the flux decreases, although not so noticeable as in the case of IC 342 source 1. In fact, when we fitted the two subgrouped spectra simultaneously by constraining $N_{\rm H}$ and $R_{\rm in}$ to take the same value between them (while allowing $T_{\rm in}$ to take separate values), we obtained an acceptable fit of χ^2/ν=140.4/126, and letting $R_{\rm in}$ to be free does not improve the fit significantly (χ^2/ν=138.0/125). Therefore $R_{\rm in}$ is consistent with being the same between the two spectra, although a weak anti-correlation between $T_{\rm in}$ and Rin may be present.

6.5 NGC 1313 Source B

NGC 1313 was observed twice with *ASCA*, in 1993 July and 1995 November (Table 4.1). Thus, like M81, this galaxy is suitable to investigate the long-term variability of the three luminous sources involved, source A, source B, and SN1978k (§ 4.2). The first observation was already reported by Petre et al. (1994), who analyzed the spectra of the three sources using power-law, TBS, and R-S models. In this thesis, we study both observations and perform more detailed spectral analysis. Among the three luminous sources, we describe source B in this section, and source A, which showed time variability in the second observation, in the next section. We study SN 1978K in § 6.9 together with other luminous extragalactic SNRs.

Table 6.6: Fitting results of the individual SIS spectra of M81 X-6 using single component models.

date	Model	$N_{\rm H}$ (10^{22}cm^{-2})	Parameters[a]	$f_{\rm X}$ (0.5–10 keV[b])	χ^2/ν (confidence level)
1994 Apr.					
	power-law	0.40±0.10	1.79±0.17	3.42	53.6/42 (11%)
	TBS	0.32±0.09	$7.1^{+3.2}_{-1.8}$	3.20	47.8/42 (25%)
	R-S[c]	$0.31^{+0.10}_{-0.06}$	$7.2^{+3.2}_{-2.0}$	3.23	47.8/41 (22%)
	MCD	0.19±0.06	1.63±0.19	2.94	43.8/42 (40%)
1994 Oct.					
	power-law	$0.48^{+0.12}_{-0.09}$	1.90±0.15	3.68	58.8/47 (12%)
	TBS	0.38±0.08	$5.6^{+1.6}_{-1.1}$	3.45	45.8/47 (52%)
	R-S[c]	0.38±0.08	$5.7^{+1.5}_{-0.8}$	3.45	45.9/46 (48%)
	MCD	0.23±0.06	1.51±0.14	3.23	34.9/47 (90%)
1995 Apr.					
	power-law	$0.42^{+0.23}_{-0.17}$	$1.77^{+0.27}_{-0.24}$	3.45	33.9/23 (7%)
	TBS	$0.33^{+0.17}_{-0.14}$	$7.5^{+7.0}_{-2.6}$	3.28	31.6/23 (11%)
	R-S[c]	$0.36^{+0.20}_{-0.16}$	$7.1^{+7.0}_{-2.8}$	3.28	31.5/22 (9%)
	MCD	$0.14^{+0.15}_{-0.11}$	1.73±0.27	3.09	29.6/23 (16%)
1995 Oct.					
	power-law	$0.34^{+0.14}_{-0.11}$	2.0±0.23	2.43	18.4/21 (62%)
	TBS	0.23±0.10	$4.7^{+2.3}_{-1.2}$	2.28	16.4/21 (75%)
	R-S[c]	0.23±0.09	$4.6^{+2.2}_{-1.1}$	2.29	16.0/20 (72%)
	MCD	0.08±0.08	$1.34^{+0.23}_{-0.18}$	2.12	17.7/21 (67%)
1996 Apr.					
	power-law	$0.78^{+0.34}_{-0.24}$	$2.31^{+0.32}_{-0.28}$	2.26	80.3/54 (1%)
	TBS	$0.57^{+0.23}_{-0.17}$	$3.4^{+1.2}_{-0.8}$	2.11	69.8/54 (7%)
	R-S[c]	$0.56^{+0.26}_{-0.14}$	3.5±1.0	2.12	69.9/53 (6%)
	MCD	$0.33^{+0.18}_{-0.14}$	$1.23^{+0.18}_{-0.15}$	2.02	61.6/54 (22%)
1996 Oct.					
	power-law	0.31±0.09	1.78±0.17	4.06	32.0/31 (42%)
	TBS	$0.22^{+0.09}_{-0.06}$	$7.2^{+3.6}_{-2.0}$	3.85	29.2/31 (56%)
	R-S[c]	0.23±0.08	$7.2^{+3.7}_{-2.1}$	3.85	29.2/30 (51%)
	MCD	0.08±0.07	$1.63^{+0.23}_{-0.19}$	3.56	30.2/31 (51%)
1997 May.					
	power-law	0.35±0.11	1.79±0.16	3.68	59.6/40 (2%)
	TBS	0.26±0.08	$6.8^{+2.8}_{-1.7}$	3.47	52.0/40 (10%)
	R-S[c]	$0.26^{+0.10}_{-0.07}$	$6.8^{+2.8}_{-1.8}$1.0	3.47	51.9/39 (8%)
	MCD	0.10±0.07	$1.61^{+0.19}_{-0.16}$	3.24	44.5/40 (29%)

[a] The same as Table 6.1
[b] In unit of 10^{-12} erg s^{-1} cm^{-2}.
[d] All the best fit parameters of the abundance are below 0.2 solar.

Table 6.7: Fitting results of the grouped SIS spectra of M81 X-6 using single component models.

Data group	Model	$N_{\rm H}$ (10^{22}cm^{-2})	Parameters[a]	$f_{\rm X}$ [b] (0.5–10 keV)	χ^2/ν (confidence level)
High-temperature state					
	power-law	0.41±0.05	1.83±0.07	3.69	110.0/65 (≤1%)
	TBS	0.31±0.04	$6.5^{+1.1}_{-0.8}$	3.48	83.0/65 (7%)
	R-S[c]	0.31±0.04	$6.5^{+1.1}_{-0.8}$	3.48	83.1/64 (5%)
	MCD	0.16±0.03	1.59±0.09	3.24	68.6/65 (36%)
	UC	0.26±0.06	$1.28^{+0.16}_{-0.13}$/25±3	3.22	67.3/64 (37%)
	Broken power-law	0.25±0.06	$1.33^{+0.19}_{-0.16}$/$3.24^{+0.61}_{-0.27}$/$2.5^{+0.4}_{-0.3}$	3.42	63.9/63 (45%)
Low-temperature state					
	power-law	0.52±0.12	2.12±0.17	2.36	93.0/59 (≤1%)
	TBS	0.38±0.10	4.1±0.9	2.19	79.0/59 (4%)
	R-S[c]	0.38±0.10	$4.0^{+1.1}_{-0.7}$	2.19	79.1/59 (3%)
	MCD	0.20±0.08	1.29±0.13	2.07	68.9/59 (18%)
	UC	0.20±0.15	$0.94^{+0.16}_{-0.12}$/36^{+8}_{-12}	2.02	66.8/58 (20%)
	Broken power-law	$0.25^{+0.15}_{-0.19}$	$1.37^{+0.32}_{-0.23}$/$3.42^{+0.34}_{-0.25}$/3.8±0.8	2.06	63.6/57 (25%)

[a] The same as Table 6.1.
[b] In unit of 10^{-12} erg s^{-1} cm^{-2}.
[c] The abundance has been constrained to be ≤0.12 solar for the high-temperature state spectrum, and ≤0.27 for the low-temperature state one.

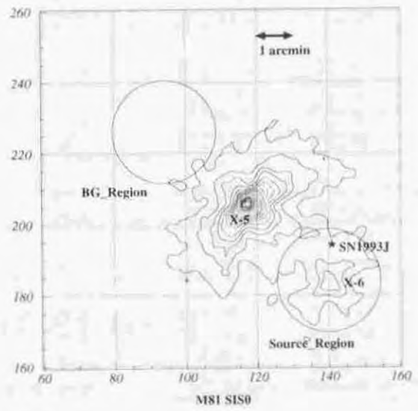

Figure 6.8: An SIS 0 image of M81 region in the 0.5–10 keV band, obtained in 1994 April. We can see X-5 and X-6 as local peaks of contours. SN 1993J had faded significantly, and we marked its position as a filled star. We also show data accumulation regions for the X-6 spectra and the background spectra.

(a) 94/04 (b) 94/10 (c) 95/04

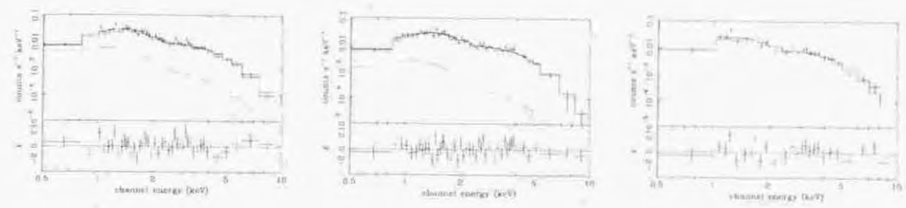

(d) 95/10 (e) 96/04 (f) 96/10

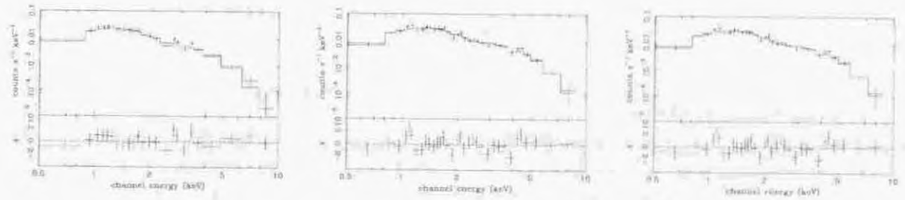

(g) 97/05

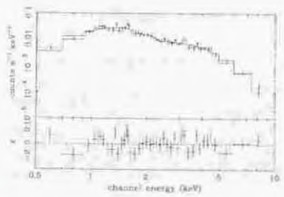

Figure 6.9: The SIS spectra of M81 X-6 acquired on seven occasions, all fitted with an MCD model. The SN 1993J contribution is taken into account only in the first two datasets (panel (a) and panel (b)), and shown as dotted lines.

High-temperature state
(a) Power-law (b) TBS (c) MCD

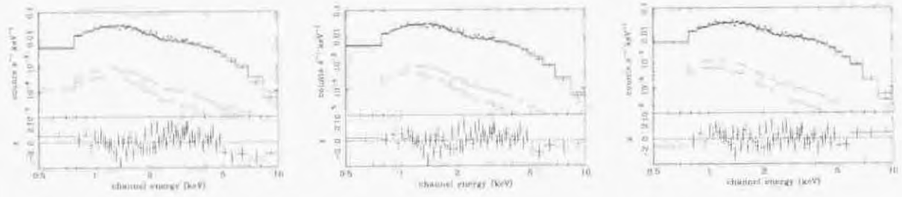

Low-temperature state
(d) Power-law (e) TBS (f) MCD

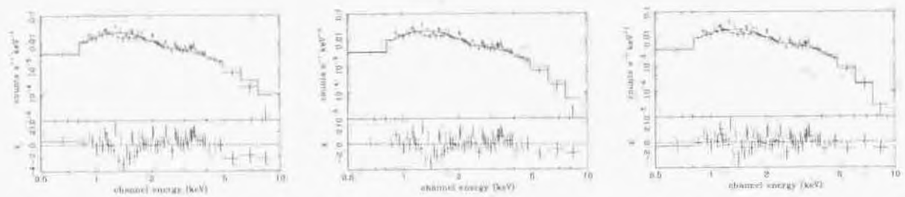

Figure 6.10: The SIS spectra of M81 X-6, obtained by grouping the individual datasets according to the values of $T_{\rm in}$. The SN 1993J contribution is taken into account as dotted lines only in the high-temperature state spectrum, which contains the 1994 observations.

(a) (b)

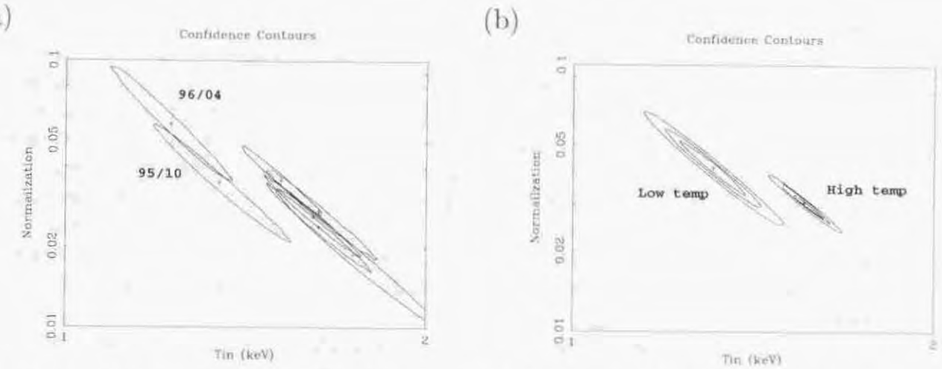

Figure 6.11: The same as Figure 6.5, but for M81 X-6 instead of IC 342 source 1. (a) The contours of individual observations, where only the 68% confidence levels are shown. (b) The contours of the high/low-temperature state spectra obtained by grouping the individual datasets. The 68%, 90%, and 99% confidence levels are shown. We fixed $N_{\rm H}$ at 1.8×10^{21} cm^{-2}.

6.5.1 1993 observation

We extracted the SIS and GIS spectra from a circular region having 3′ radius, the same as utilized previously by Petre et al. (1994), and the background spectra from blank-sky observations. We fitted the background-subtracted spectra with our typical single component models. The obtained results, which are summarized in Table 6.8 and Figure 6.12, are similar to those of IC 342 source 1 and M81 X-6; the power-law model is unacceptable, the TBS and R-S models are acceptable (within 95% confidence) but require rather large values of $N_{\rm H}$ compared to the Galactic line-of-sight column density ($N_{\rm H}$=3.5×10^{20}cm^{-2}), whereas the MCD model is fully satisfactory. Although the UC and broken-power-law models also provide as low χ^2 as the MCD model does, $N_{\rm H}$ is again rather high.

The presence of hard components is, again, insignificant. The reduction of χ^2 is below 0.1 for both the Γ = 2.2 power-law and the kT=2.0 keV black body modelings. Even when we include these hard components at the allowed upper limit (90% confidence), their contribution to the 0.5–10 keV flux is only 25% and 21% for the power-law and the black-body modelings, respectively. Therefore the single MCD model is likely to be the best representation of the data.

6.5.2 1995 observation

We extracted the source spectra in the same way as the first observation. The SIS was operated in a 1-CCD mode (Table 4.1), so that we derived the SIS background spectrum from a source-free region of the on-source data. Since the GIS data were acquired in an exceptional operation mode which sacrifices rise-time information to improve the time resolution (in search for a pulsar in SN1978k), we cannot apply the off-line rise-time cut screening to the data (§ 3.4.2). Therefore we extracted the GIS background spectrum

from blank-sky observations without applying the off-line rise-time cut, too.

The obtained SIS/GIS spectra have been fitted jointly with our typical single component models, in the same way as for the 1993 data. The fitting results are summarized in Table 6.8 and Figure 6.12, together with those of the first observation. Thus, the flux decreased to ∼40% of the 1993 value in two years, regardless of the assumed models. Comparison among the five single-component models leads us to the same conclusion as was obtained for IC 342, M81 X-6, and the 1993 data of NGC 1313 source B. That is, the MCD model is best preferred based on the χ^2 goodness as well as the smallness of $N_{\rm H}$. Data do not require separate hard components, with the Γ=2.2 power-law and the kT=2.0 keV black-body contributing at most 58% and 24% to the 0.5–10 keV source flux, respectively.

Since the MCD model is likely to be the best model to represent the data, for both the 1993 observation and the 1995 observation, we plotted the confidence contours in the $T_{\rm in}$-$R_{\rm in}^2$ plane in Figure 6.13, fixing the absorption at $N_{\rm H}$=7×10^{20}cm^{-2} (the average value between the two observations). Like the two variable sources so far studied, a slight increase in $R_{\rm in}$ can be seen as the flux decreases. The change of $R_{\rm in}$ is significant, since we obtain the significantly improved fit (χ^2/ν=214.9/207) when fitting the two observation simultaneously allowing $R_{\rm in}$ to take separate values, compared with that (χ^2/ν=222.9/208) obtained when constraining $R_{\rm in}$ to be common.

Table 6.8: Joint fit results of the SIS/GIS spectra of NGC 1313 source B using single component models.

data	Model	$N_{\rm H}$ (10^{22}cm^{-2})	Parameter[a]	$f_{\rm X}$ [b] (0.5–10 keV)	χ^2/ν (confidence level)
1993 Jul.					
	power-law	0.40±0.07	1.99±0.09	3.91	174.2/130 (≤1%)
	TBS	0.26±0.05	$5.1^{+0.8}_{-0.6}$	3.73	143.2/130 (20%)
	R-S[c]	0.26±0.06	$5.1^{+0.8}_{-0.6}$	3.73	143.4/129 (18%)
	MCD	0.08±0.04	1.47±0.08	3.59	124.5/130 (62%)
	UC	0.16±0.08	$1.13^{+0.15}_{-0.10}/27^{+5}_{-4}$	3.54	125.6/129 (57%)
	Broken power-law	0.17±0.08	$1.40\pm0.18/3.35^{+0.32}_{-0.35}/2.81^{+0.34}_{-0.29}$	3.72	126.2/128 (53%)
1995 Nov.					
	power-law	0.44±0.08	2.46±0.13	1.51	110.3/74 (≤1%)
	TBS	0.23±0.06	2.9±0.4	1.44	91.8/74 (8%)
	R-S[c]	0.23±0.06	2.9±0.4	1.44	91.9/73 (7%)
	MCD	0.06±0.05	1.07±0.07	1.39	89.8/74 (10%)
	UC	0.20±0.10	$0.97\pm0.13/24^{+6}_{-5}$	1.40	89.6/73 (9%)
	Broken power-law	0.24±0.10	$1.86\pm0.25/3.06^{+0.49}_{-0.42}/3.28^{+0.61}_{-0.43}$	1.45	87.9/72 (10%)

[a] The same as Figure 6.1.
[b] In unit of 10^{-12} erg s^{-1} cm^{-2}.
[c] The abundance has been constrained to be ≤0.06 solar for the 1993 observation, and ≤0.08 solar for the 1995 observation.

6.6 NGC 1313 Source A

As mentioned in § 5.2, this ULX showed flux decrease during the second observation. Therefore, we first analyze the time-averaged spectrum of each observation, and then investigate the short-term spectral variability in the second observation.

(a) 93/7 Power-law

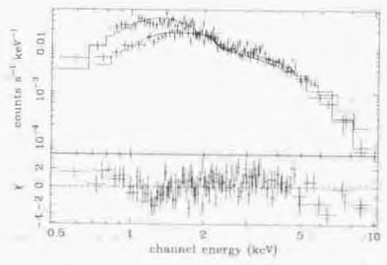

(b) 95/11 Power-law

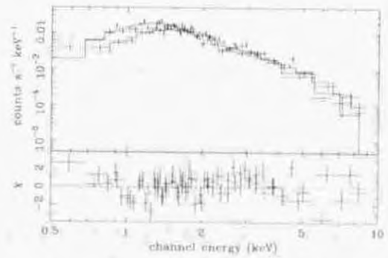

(c) 93/7 TBS

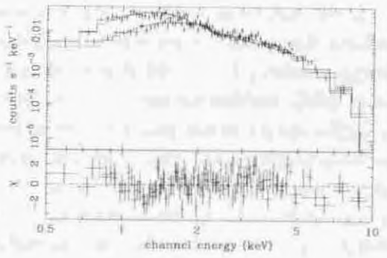

(d) 95/11 TBS

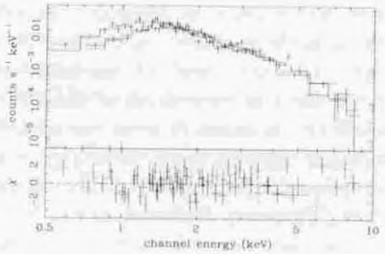

(e) 93/7 MCD

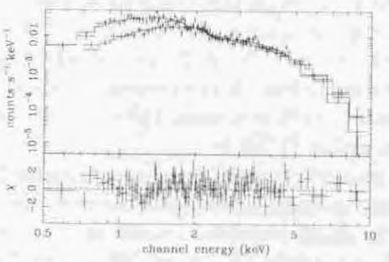

(e) 95/11 MCD

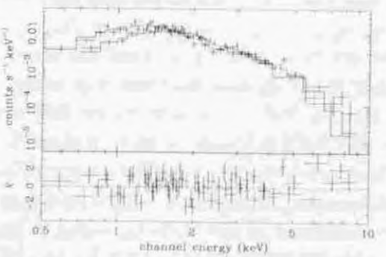

Figure 6.12: The SIS and GIS spectra of NGC 1313 source B, jointly fitted with single component models.

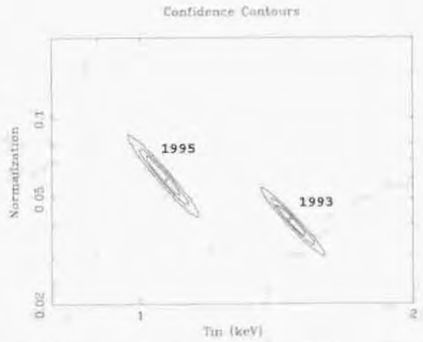

Figure 6.13: The same as Figure 6.5, but for the NGC 1313 source B instead of IC 342 source 1. We fixed the photoelectric absorption at $N_{\rm H}$=7×10^{20}cm^{-2}.

6.6.1 Averaged spectra of each observation

We extracted the source and background spectra in the same way as for source B. We fitted the spectra in the same way as before, and obtained the results as presented in Table 6.9 and Figure 6.14. Our spectral parameters of the power-law, TBS, and R-S models in the 1993 observation agree with those of Petre et al. (1994) within the statistical errors.

The results on source A are noticeable, because the MCD model gives the worst fit and is statistically rejected (99% confidence) for the 1993 observation, like M33 X-8. Instead, the power-law and TBS (or most identical R-S) models are acceptable for both 1993 and 1995 data. However, representing the spectra of source A by these models is not fully satisfactory; the obtained values of $N_{\rm H}$ somewhat contradict the Galactic line-of-sight column density ($N_{\rm H}$=3.5×10^{20}cm^{-2}) for the TBS and R-S modelings of the 1993 data. Moreover, either model provides inconsistent values of the absorption between the 1993 and 1995 observation, although it does not necessarily means a problem.

Thus, we suspect that the spectra of source A had changed, for two years, not only in its hardness but also in its composition, and this causes the apparent change of $N_{\rm H}$. In order to compare the spectra of the two observations in a model-independent manner, we plotted "unfolded" (detector efficiency removed) spectra of the two observations in Figure 6.15. It implies that the flux in the soft-energy band had increased for two years, while that in the hard-energy band had decreased. Such a spectral behavior reminds us of the soft-hard transitions seen in the Galactic BHBs (§ 2.3.4).

Therefore we refitted the data with a single power-law model or a power-law plus MCD model, corresponding to the hard and soft state spectra of BHBs respectively, with the absorption fixed at the Galactic value. Using the single power-law model, we obtained an acceptable fit (χ^2/ν=114.8/152) for the 1993 spectra with Γ=1.69±0.05, a typical value for the BHBs in the hard state. On the other hand, the fit failed (χ^2/ν=170.8/101) for the 1995 datasets and the fit residuals, which is shown in Figure 6.16a, indicate that the actual spectra has a convex shape in the 1–5 keV band so that the power-law model is too "straight" to represent the data. This is also evident from the unfolded spectra of Figure 6.15b. We hence added a MCD component for the 1995 data, to make the spectrum more "convex" in the low-energy band, and obtained an acceptable fit of χ^2/ν=91.9/99.

We summarize the fitting results in Table 6.10 and Figure 6.16; the obtained parameters have typical values for the soft-state BHBs. We hence adopt the single power-law model and the power-law plus MCD model to describe the spectra of the 1993 observation and the 1995 one respectively, although we cannot reject statistically other modelings such as the power-law model with absorption which is allowed to change.

6.6.2 Variability in the second observation

Since the flux of the source showed a monotonic decrease, we divided the data into two parts; the former half and the latter half, as shown in Figure 5.5, and accumulated the individual spectra. In order to obtain a crude information of the spectral variability, we first make a count-rate ratio between the two datasets. As shown in Figure 6.17, the decrease of the source intensity is noticeable in the high-energy band. This suggests that the hard band power-law component changed, while the soft MCD component stayed constant. To confirm this insight, we fitted the two sets of spectra with the power-law plus MCD model, fixing Γ and $T_{\rm in}$ at the best-fit value of the averaged spectra to obtain a stable fitting. The results are summarized in Table 6.10 and Figure 6.18. Thus, the flux of the power-law component significantly decreased by $\sim$ 30% from the former period to the latter one, whereas that of the MCD component is almost constant; this agrees with the implication of Figure 6.17. This behavior, i.e. variation of the hard component with little change of the MCD component, is often seen from soft-state BHBs.

In this way, the long-term variation of source A can be interpreted as a soft-hard state transition of a BHB (except for the higher flux in the hard state), and its short-term variability in 1995 can be described as a change in the hard-tail component. These results support the BH interpretation of source A. We note that the value of $T_{\rm in}$=0.67 keV of this object (Table 6.10) is comparable to those of Galactic and Magellanic BHBs, while significantly lower than those of other ULXs.

Table 6.9: Summary of the spectral fitting results of NGC 1313 source A. The SIS/GIS spectra are fitted jointly with our typical single component models.

date	Model	$N_{\rm H}$ (10^{22}cm^{-2})	Γ or kT or $T_{\rm in}$ (keV)	$f_{\rm X}$ [a] (0.5–10 keV)	χ^2/ν (confidence level)
1993 Jul.					
	power-law	0.10±0.04	1.79±0.07	3.95	109.5/151 (99%)
	TBS	≤0.03	7.5±1.0	3.87	107.8/151 (99%)
	R-S[b]	≤0.04	7.3±1.0	3.87	107.2/151 (99%)
	MCD	≤0.01	1.43±0.06	3.27	216.0/151 (≤1%)
1995 Nov.					
	power-law	0.36±0.06	2.81±0.14	2.96	88.6/100 (79%)
	TBS	0.11±0.05	$2.0^{+0.3}_{-0.2}$	2.89	91.7/100 (71%)
	R-S[b]	0.11±0.05	$2.0^{+0.3}_{-0.2}$	2.91	91.5/99 (69%)
	MCD	≤0.02	0.82±0.04	2.74	117.8/100 (11%)

[a] In unit of 10^{-12} erg s^{-1} cm^{-2}.
[b] The best fit abundance is 0.08(≤0.27) solar for the 1993 observation, and 0.04(≤0.12) solar for the 1995 observation.

(a) 93/7 Power-law

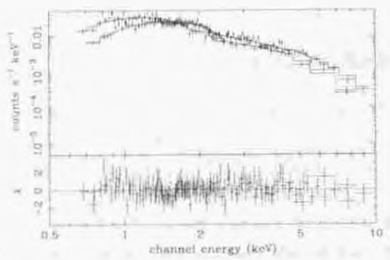

(b) 95/11 Power-law

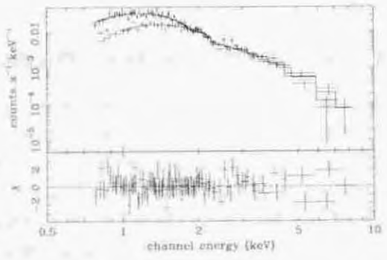

(c) 93/7 TBS

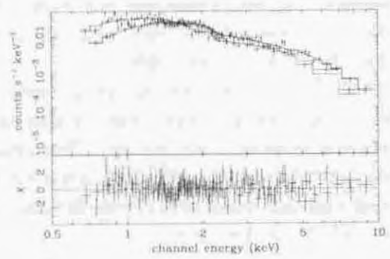

(d) 95/11 TBS

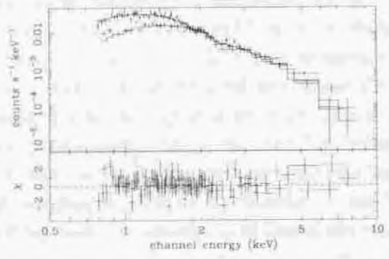

(e) 93/7 MCD

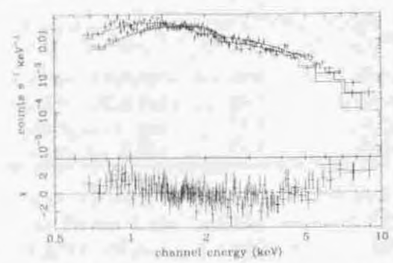

(e) 95/11 MCD

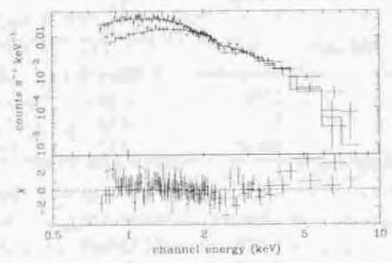

Figure 6.14: The same as Figure 6.12, but for NGC 1313 source A instead of source B.

Table 6.10: Joint fit results of the SIS/GIS spectra of NGC 1313 source A in the second observation. The spectra are fitted with the power-law plus MCD model.

Period	$N_{\rm H}$ (10^{22}cm^{-2})	Γ	$f_{\rm X}^{\rm hard\ a)}$ (0.5–10 keV)	$T_{\rm in}$ (keV)	$f_{\rm X}^{\rm soft\ a)}$ (0.5–10 keV)	χ^2/ν (confidence level)
Average	0.035(fix)	$1.74^{+0.31}_{-1.02}$	1.38	$0.67^{+0.08}_{-0.06}$	1.78	91.9/99 (68%)
Former	0.035(fix)	1.74(fix)	1.60	0.67(fix)	1.82	68.8/64 (32%)
Latter	0.035(fix)	1.74(fix)	1.12	0.67(fix)	1.75	56.1/55 (43%)

a) In unit of 10^{-12} erg s^{-1} cm^{-2}.

(a) Unfolded spectra of the SIS

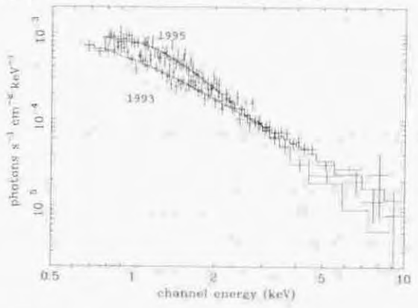

(b) Unfolded spectra of the GIS

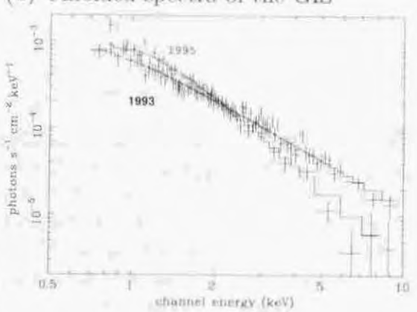

Figure 6.15: Changes of the source A spectra from the 1993 observation to the 1995 one. We show the "unfolded" (detector efficiency removed) spectra for direct comparison. The histograms represent the best-fit power-law model of Table 6.9. The spectrum of the 1995 observation shows higher flux in the low-energy band.

(a) Single power-law

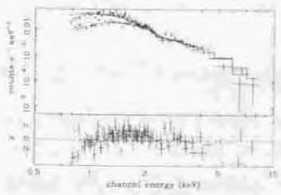

(b) PL+MCD SIS

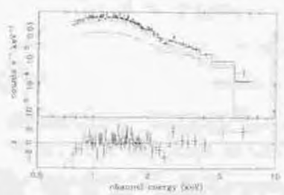

(c) PL+MCD GIS

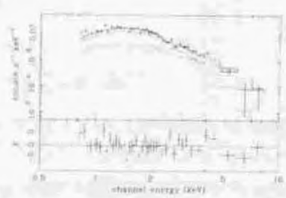

Figure 6.16: The spectra of source A in the 1995 observation, fitted jointly with the single power-law model or the power-law plus MCD model. In the latter case, the contribution of each component is shown as dotted lines, and the SIS/GIS spectra are separately displayed for clarify.

(a) SIS (b) GIS

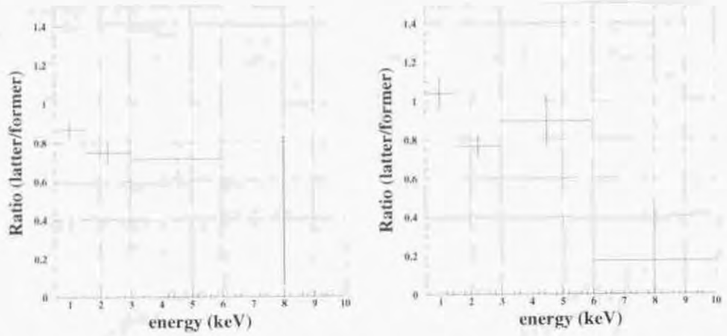

Figure 6.17: The count-rate ratio between the former and the latter half of the 1995 observation of NGC 1313 source A.

(a) The former half (b) The latter half

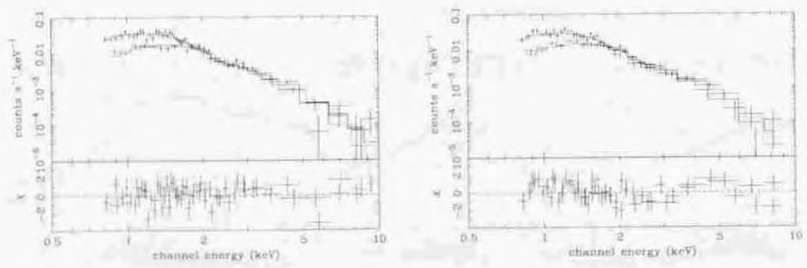

Figure 6.18: The SIS/GIS spectra of source A in the 1995 observation, jointly fitted with the power-law plus MCD model. Panel (a) represents the spectra obtained in the former-half period, while (b) represents the spectra of the latter-half one.

6.7 NGC 4565

This edge-on galaxy has two luminous sources, as already mentioned in § 4.2; one is $\sim 0'.8$ above the galaxy disk, while the other is positionally coincident with the galactic nucleus, as shown in Figure 6.19 (see also images in Appendix C). Because of a short separation ($\sim 0'.8$) of these two sources, we first analyze the summed energy spectra in § 6.7.1, and then investigate the individual spectra in § 6.7.2. These results have already been published as Mizuno et al. (1999).

6.7.1 Summation of the two sources

Before extracting the summed energy spectra, we investigate the hardness of two sources, in order to grasp rough spectral properties of them. We projected the SIS events inside the rectangle of Figure 6.19 onto its longer side. The derived one-dimensional X-ray profiles are shown in Figure 6.20, in three representative energy bands. Each profile is fitted by the projected PSF of the XRT convolved with the two point sources of which the projected positions are fixed at those indicated by the ROSAT image. We assumed a constant background and determined the intensity of the two sources in the three energy band, as tabulated in Table 6.11. Thus, the intensity ratios of the two sources are energy independent within statistical errors, indicating that the two sources have similar spectra, as reported by Mizuno et al. (1999). We therefore accumulated events over circular regions of radius $4'$ and $6'$ for the SIS and the GIS, respectively, both centered on the off-center (brighter) source but including the other source as well. The obtained spectra, which co-add photons from the two sources, are fitted with single-component models, as summarized in Table 6.12 and Figure 6.21a. For the spectral fitting, we used the response function for a point source located at the off-center source.

Like most of the sources we studied so far, the power-law model is completely unacceptable, the TBS and R-S models give better fits but require large absorption compared with the Galactic $N_{\rm H}$ ($1.3\times10^{20}{\rm cm}^{-2}$), whereas the MCD model shows the lowest χ^2 and a reasonable value of $N_{\rm H}$. The data also need no additional hard components, and their contribution to the 0.5–10 keV flux is at most (90% confidence) $\sim$30% for both the Γ=2.2 power-law and the kT=2.0 keV black-body component. In short, when the spectra of the two objects are added together, the results can be represented well by an MCD model of $T_{\rm in}$ $\sim$1.4 keV, as already pointed out by Mizuno et al. (1999).

6.7.2 Individual sources

As a further investigation, we attempted to estimate the spectra of the two sources individually, after Mizuno et al. (1999). We therefore fitted the same SIS and GIS spectra jointly with a sum of two MCD components having separate temperatures, separate normalizations, and separate column densities, which were all left free to vary. In order to ensure that the two model components are well determined, we imposed additional constraints that each MCD component should correctly reproduce the three-band coarse spectrum of the corresponding source, which was produced by converting the count rates in Table 6.11. The response function to represent the three-band spectra was made by scaling and rebinning the response function used in the previous subsection. As a result, we jointly fitted four spectra (whole spectrum of the SIS, that of the GIS, three-band

SIS spectrum for the off-center sources, and that for the center source) and determined the model parameters to minimize the total chi-square. We show these four spectra in Figure 6.21b.

This composite model have given an acceptable fit with χ^2/ν=147.7/124. The obtained results, summarized in Table 6.13, imply that the two sources exhibit the same disk temperature within errors, which in turn agree with that derived in Table 6.12. This justifies our analysis performed in the previous subsection. Neither source exhibits detectable absorption, again in agreement with Table 6.12. Even when we represent the center source spectrum by a power-law model, its absorption remains rather low, $N_{\rm H} \leq 2\times10^{21}{\rm cm}^{-2}$. This fact contradicts the interpretation that the center source is an LLAGN located at the galactic nucleus, since the column density along the galactic disk to the nucleus of such an edge-on galaxy (i=86°, Hummel et al. 1984) would amount to at least $\sim1\times10^{22}{\rm cm}^{-2}$. Thus, we regard both the off-center and center sources as ULXs, as already reported by Mizuno et al. (1999). Their disk temperatures, $T_{\rm in}$, are ~1.5 keV, similar to those of M81 X-6 and NGC 1313 source B in the 1993 observation.

Table 6.11: Observed count rates (in 10^{-2} c s^{-1}) of the two sources in NGC 4565.[a) b)]

Source	soft (0.5–1.5 keV)	medium (1.5–3 keV)	hard (3–10 keV)
Off-center	1.41±0.10	1.24±0.09	0.64±0.07
Center	0.54±0.09	0.37±0.07	0.27±0.06
Ratio[c)]	2.61±0.47	3.35±0.68	2.37±0.59

a) Count rate of the event inside the rectangle shown in Figure 6.19, obtained through fitting to the one-dimensional profile of Figure 6.20.
b) Errors represent one-sigma statistical errors, instead of the 90% confidence limit.
c) Count rate ratio of the off-center source to the center one.

Table 6.12: Results of the joint fits to the SIS and GIS spectra of NGC 4565 [a)] with single component models.

Model	$N_{\rm H}$ (10^{22} cm^{-2})	Γ or T or $T_{\rm in}$ (keV)	$f_{\rm X}$ [b)] (0.5–10 keV)	χ^2/ν (confidence level)
Power-law	0.25±0.05	$1.89^{+0.09}_{-0.08}$	2.64	174.2/121 (≤1%)
TBS	0.14±0.04	$5.6^{+0.9}_{-0.7}$	2.47	152.4/121 (3%)
R-S[c)]	0.14±0.04	$5.5^{+0.9}_{-0.7}$	2.47	152.3/120 (2%)
MCD	≤ 0.02	$1.43^{+0.07}_{-0.06}$	2.32	145.9/121 (6%)

a) Spectra of the two sources are co-added together.
b) In units of 10^{-12} erg s^{-1} cm^{-2}.
c) The abundance has been constrained to be ≤ 0.1 solar.

Table 6.13: Estimates of the spectra of the individual sources in NGC 4565.[a)]

Source	$N_{\rm H}$ (10^{22} cm^{-2})	$T_{\rm in}$ (keV)	$f_{\rm X}$ [b)] (0.5–10 keV)
Off-center	≤0.02	1.39±0.08	1.65
Center	≤0.05	$1.59^{+0.32}_{-0.23}$	0.67

a) The SIS/GIS spectra of NGC 4565 were fitted jointly with two MCD components, which are constrained to reproduce the count rates in Table 6.11.
b) In unit of 10^{-12} erg s^{-1} cm^{-2}.

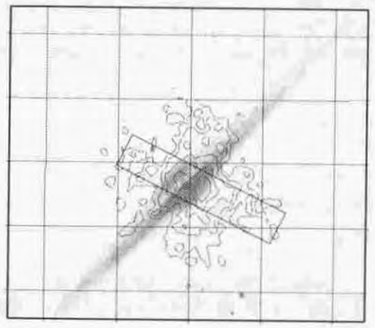

Figure 6.19: *ASCA* SIS image of NGC 4565, superposed on the optical image (Digital Sky Survey). A rectangle in the image is used to make one-dimensional X-ray profiles (see text). See also Appendix C, where the *ROSAT* HRI and GIS images are shown.

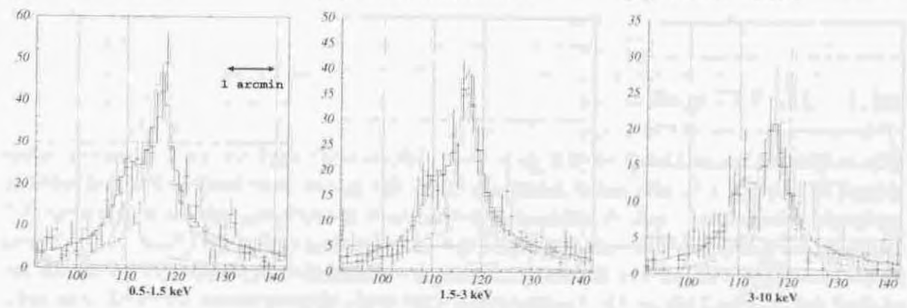

Figure 6.20: The projected one-dimensional X-ray brightness distribution of NGC 4565, in 0.5–1.5 keV (panel a), 1.5–3 keV (panel b), and 3–10 keV (panel c). The SIS events within the rectangle of Figure 6.19 are used. The dotted, dashed, and dot-dashed lines indicate the model for the center-source, that for the off-center source, and a constant background, respectively.

(a) Single MCD (b) Two MCDs

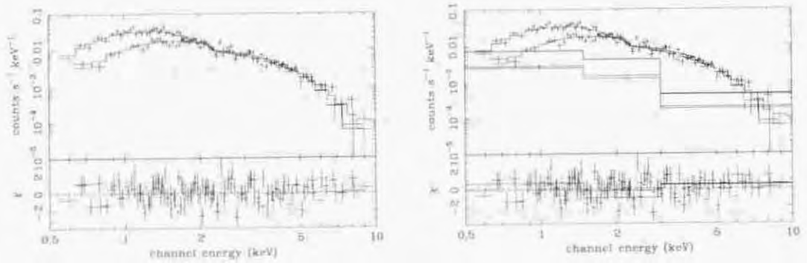

Figure 6.21: The SIS and GIS spectra of NGC 4565, dominated by the two sources. Panel (a) represents the fit with a single MCD model, and panel (b) represents the fit with two MCD models, incorporating the constraints that each model can simultaneously reproduce the three-band spectrum (data points with wide bin) of the corresponding source, which is derived from Table 6.11.

6.8 Other ULXs

We study all remaining ULXs together in this section, since they have rather poorer photon statistics, or do not show significant features, such as time variability, which require detailed analysis. We only use our basic single component models; a power-law, a TBS, a R-S, or an MCD model, to fit their spectra. All the fitting results are summarized in Table 6.14 and Figure 6.22.

6.8.1 IC 342 source 2

This is the second brightest source in IC 342. We accumulated the spectra in the same way as for source 1 in the same galaxy (§ 6.2). All of our four models are statistically acceptable, and the obtained fitting parameters are consistent with those reported by Okada et al. (1998). Although the MCD model provides the lowest χ^2/ν, the obtained temperature ($T_{\rm in}$ $\sim$3 keV) is uncomfortably high compared with those of other ULXs we studied so far. The TBS and R-S models also show quite high temperature of kT $\geq$30 keV, well beyond the high-energy end of the *ASCA* band. These facts mean that the actual data has a straight shape in logalithmic plot, and obtained high temperatures might be artifacts. We consider that the power-law model best represent the spectrum of IC 342 source A, although the other models cannot be rejected. The obtained photon index, Γ=1.47$\pm$0.17, is similar to those of BHBs in high-state, so that the source, like NGC 1313 source A in the 1993 observation, can be explained as a BHB in high state. Regardless of the assumed model, this source shows high absorption ($N_{\rm H}$ $\geq$$10^{22}$cm^{-2}), well beyond the Galactic line-of-sight column density ($N_{\rm H}$=3$\times$$10^{21}$cm^{-2}).

6.8.2 NGC 2403 source 3

This, the brightest source in NGC 2403, has been known as ULX since the *Einstein* era (§ 4.2). We extracted the SIS and GIS spectra from a circular region of 2′ radius, slightly smaller than usual, to avoid contamination from nearby weak sources (see *ASCA* images in Appendix C). Spectral fitting results are similar to those obtained from most of our sample objects; the MCD model best represents the data judging on the χ^2 goodness, and provides reasonable value of $N_{\rm H}$ compared with the Galactic absorption ($N_{\rm H}$=4$\times$$10^{20}$cm^{-2}). The obtained value of $T_{\rm in}$, $\sim$1.2 keV, is similar to that of M33 X-8.

6.8.3 Dwingeloo 1 X-1

As mentioned in § 4.2, this galaxy was newly discovered behind the Milky way (Kraan–Korteweg et al. 1994), and Reynolds et al. (1997) found an off-center source, namely Dwingeloo 1 X-1, with *ASCA*. We used a 3′ radius circle to extract the source spectra. Since the source is located on the Galactic plane as mentioned in § 4.2, we extracted the background spectrum from on-source data not only for the SIS but also for the GIS. The obtained parameters of the power-law, TBS, and R-S model fittings are consistent with those of Reynolds et al. (1997), and all these three models as well as the MCD one produce similar values of χ^2, probably because of rather poor photon statistics. However, the MCD model is somewhat preferred; it provides the value of $N_{\rm H}$ comparable to the Galactic line-of-sight column density ($N_{\rm H}$=7$\times$$10^{21}$), whereas the others require excess absorption. The obtained value of $T_{\rm in}$ is as high as that of IC 342 source 1.

6.8.4 NGC 1365 SW source

This source is located close ($\sim$1.′2) to the galaxy nucleus, an LLAGN of the host galaxy. In order to avoid the contamination from the nucleus as much as possible, we used only the SIS data which has a higher spatial resolution than the GIS, and we reduced the radius of the source-extracting region to 1.′5. In addition, we shifted the integration center from the source center by $\sim$1′ to the direction opposite to the nucleus. The background subtraction is performed in the same way as for M81 X-6, in order to remove the contaminating photons from the nucleus. Because of quite poor statistics, we cannot tell which model is preferred based on the values of χ^2, as indicated by Table 6.14. If we adopt the MCD model to describe the spectrum, the source shows a similar value of $T_{\rm in}$ to other ULXs, such as M81 X-6, NGC 1313 source B in the 1993 observation, and two ULXs in NGC 4565. The source flux we obtained is $\sim$40% of that reported by Iyomoto et al. (1997), mainly because they used blank-sky data to extract the background spectrum, whereas we used the on-source data and thus subtracted the contamination from the nucleus source. The spectrum reported by Iyomoto et al. (1997) was too hard for the same reason.

6.8.5 NGC 3628 off-center source

The source unfortunately fell on the inter-chip gap of the SIS, so that we used only the GIS data. Since the source has the lowest flux among our objects, we extracted the spectrum from a circular region of rather small radius, 2′; using a larger region makes the S/N ratio worse. Like NGC 1365 SW source, all our models provide similar values of χ^2, and spectral parameters of the power-law and TBS models are consistent with those reported

by Yaqoob et al. (1995). Regardless of the assumed model, the obtained spectrum shows excess absorption above the Galactic line-of-sight column density, $N_{\rm H}$=2×10^{20}cm^{-2}. If we employ the MCD model, the best-fit value of $T_{\rm in}$ ($\sim$1.1 keV) is similar to that of M33 X-8 and NGC 2403 source 3, although the statistical error is relatively large.

Table 6.14: Fitting results of remaining ULXs, using single component models.

Source	Model	$N_{\rm H}$ (10^{22}cm^{-2})	Γ or kT or $T_{\rm in}$ (keV)	$f_{\rm X}$ [a] (0.5–10 keV)	χ^2/ν (confidence level)
IC 342 source 2					
	power-law	1.43 ± 0.16	1.39 ± 0.10	4.14	102.8/87 (12%)
	TBS	1.35 ± 0.13	37^{+40}_{-14}	4.10	100.1/87 (14%)
	R-S[b]	1.35 ± 0.13	37^{+27}_{-14}	4.10	100.0/87 (14%)
	MCD	0.99 ± 0.09	$3.03^{+0.38}_{-0.24}$	3.95	96.4/87 (23%)
NGC 2403 source 3					
	power-law	0.47 ± 0.11	$2.23^{+0.16}_{-0.13}$	1.66	85.7/58 (1%)
	TBS	0.29 ± 0.08	3.7 ± 0.6	1.57	71.0/58 (12%)
	R-S[b]	0.29 ± 0.08	3.6 ± 0.5	1.58	71.1/57 (10%)
	MCD	0.11 ± 0.07	1.23 ± 0.10	1.50	64.9/58 (25%)
Dwingeloo 1 X-1					
	power-law	$1.23^{+0.32}_{-0.28}$	1.87 ± 0.26	0.90	64.4/59 (29%)
	TBS	$1.04^{+0.23}_{-0.20}$	$7.3^{+3.8}_{-2.1}$	0.86	63.9/59 (33%)
	R-S[b]	$1.03^{+0.26}_{-0.20}$	$7.4^{+5.1}_{-2.7}$	0.86	63.3/58 (30%)
	MCD	0.75 ± 0.18	$1.80^{+0.33}_{-0.26}$	0.80	64.0/59 (31%)
NGC 1365 SW source					
	power-law	$0.84^{+0.74}_{-0.59}$	$2.00^{+0.57}_{-0.64}$	0.45	8.8/10 (55%)
	TBS	$0.62^{+0.73}_{-0.40}$	$5.5^{+37.2}_{-1.4}$	0.43	8.9/10 (55%)
	R-S[b]	$0.63^{+0.95}_{-0.44}$	$5.4^{+36.0}_{-3.2}$	0.43	8.9/9 (45%)
	MCD	$0.37^{+0.61}_{-0.35}$	$1.51^{+1.04}_{-0.47}$	0.39	9.3/10 (51%)
NGC 3628 off-center					
	power-law	$1.14^{+0.91}_{-0.79}$	$2.61^{+0.91}_{-0.59}$	0.39	5.4/12 (84%)
	TBS	$0.71^{+0.68}_{-0.45}$	$2.9^{+3.2}_{-1.3}$	0.36	5.2/12 (95%)
	R-S[b]	$0.71^{+0.77}_{-0.48}$	$2.9^{+4.1}_{-1.3}$	0.36	5.2/12 (92%)
	MCD	$0.42^{+0.42}_{-0.21}$	$1.12^{+0.55}_{-0.41}$	0.34	5.2/12 (91%)

[a] In unit of 10^{-12} erg s^{-1} cm^{-2}.
[b] The best-fit values of the abundance are below 0.1 solar for all the sources.

6.9 SNRs

Among our sample objects, we finally analyze the X-ray luminous extragalactic young SNRs; north-arm SNR in NGC 6946, SN 1978K in NGC 1313, and SN 1986J in NGC 891. Our aim is to compare these SNRs with ULXs so far studied, but not to study their detailed emission mechanism. Therefore, we focus on their X-ray spectral properties, and do not mention their detailed features in other wavebands. Before performing the spectral fitting of each source, we plot their unfolded spectra in Fiugre 6.23. By comparing them with the unfolded spectra of IC 342 source 1 in Figure 6.2, we can see distinctive features of these extragalactic SNRs in a model independent manner as below. North-arm SNR in

(a) IC 342 source 2

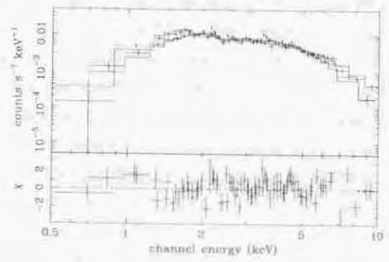

(b) NGC 2403 source 3

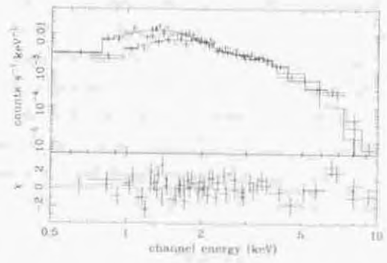

(c) Dwingeloo 1 X-1

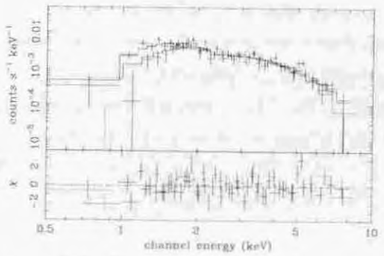

(d) NGC 1365 SW source

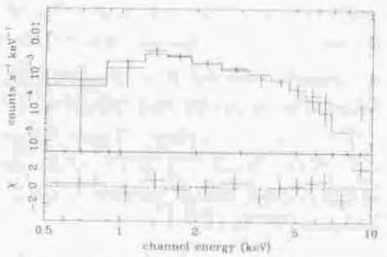

(e) NGC 3628 off-center

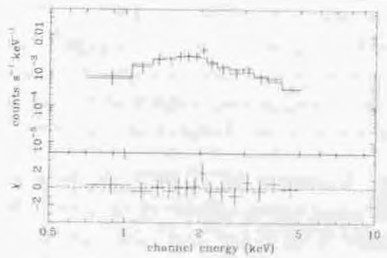

Figure 6.22: The spectra of remaining ULXs, fitted with single component models. We used only the SIS data for NGC 1365 SW source, and the GIS data for NGC 3628 off-center source. The spectra of IC 342 source 2 are fitted with a power-law model, while all the other sources are fitted with an MCD model.

NGC 6946 and SN 1978K have rather straight shape in the high-energy band, implying that a non-thermal emission, such as synchrotron radiation, is the emission mechanism. Although SN 1986J has relatively convex curvature like IC 342 source 1, a prominent line-feature is clearly seen around 6–7 keV. We tentatively fit the spectra in the 5–10 keV band by a power-law model with a single gaussian component, and obtained the line-center energy as 6.73±0.12 keV, which can be attributed to the line emission from highly ionized iron in the optically-thin hot plasma. Thus the R-S model with a high-temperature is expected to represent the data. To confirm these features quantitatively, we fit their *ASCA* spectra, first with typical single component models, and then, if needed, test more complicated ones. These spectral fitting results are summarized in Table 6.15, Table 6.16, and Figure 6.24.

North-arm SNR in NGC 6946 This source is identified as an SNRs based on its positional coincidence by Schlegel (1994), as already described in § 4.2. *ASCA* observed NGC 6946 twice, in 1993 May and 1994 December (Table 4.1). Since the source is located near ($\sim 2'.5$) the galaxy nucleus, which exhibits X-ray emission probably because of starburst activity of the host galaxy, we analyzed only the SIS data and extracted the spectrum from $1'.5$ radius circular region. Unfortunately, the source fell on the inter-chips gap in the 1993 observation, so that we do not use this dataset.

As already inferred from Figure 6.23, the MCD model gives the worst χ^2/ν and is completely rejected (see Table 6.15). None of the other models are acceptable at 90% confidence, either. These failure of the fitting is caused by the excess in the soft-energy band ($\leq$1 keV), as shown in Figure 6.24a. This indicates the presence of a soft component, probably due to thin-thermal radiation frequently observed in Galactic SNRs (§ 2.3.1).

Accordingly, we added a R-S model as the soft component to the power-law or TBS models, and summarized the fitting results in Table 6.16. Both composite models represent the observed spectrum equally well, and the presence of these soft components is quite significant, at 99% confidence level based on an F-test. The power-law plus R-S model is somewhat preferred since the obtained $N_{\rm H}$ is consistent with the Galactic line-of-sight column density ($N_{\rm H}$=2×10^{21}cm^{-2}). Thus, the emission from NGC 6946 north-arm SNR is explained by a $\Gamma \sim 2$ power-law and a $kT \leq 1$ keV plasma emission, which can be attributed, for example, to Crab-type synchrotron radiation and shock-heated thermal emission, respectively. The 0.5–10 keV luminosity becomes 5×10^{39} erg s^{-1} at an assumed distance of 5.5 Mpc.

SN 1978K The X-ray emission from SN 1978K, located in NGC 1313, was first discovered by *ROSAT* serendipitously in a 1990 observation (Ryder et al. 1993). It was recognized as a supernova first on the basis of its X-ray and radio emission, and then optically identified as a Type II supernova which detonated in 1978 June.

We accumulated the source spectrum from $2'$ radius circular region, rather smaller than usual, in order to avoid the overlap with those for source A and source B. The background subtraction is done in the same way as for these sources.

Like NGC 6946 north-arm SNR, the MCD model is rejected for both the 1993 and 1995 observation. All the other models are acceptable for the 1993 observation, as already reported by Petre et al. (1994). However, none of our single component

models succeed for the 1995 data and there exists soft excess, again like the SNR in NGC 6946. Accordingly, we added a R-S model to the power-law or the TBS model, and obtained the results as given in Table 6.16. Thus, the presence of these soft components is significant at 99% confidence. We also added the same soft component to the data of 1993 observation, fixing the temperature and the abundance at the best-fit values of the 1995 observation to obtain a stable fitting. As indicated by Table 6.16, the presence of these soft components is also significant, although the confidence level is relatively low, at 90% when adding the soft component to the power-law model. The source flux seems to have changed from the 1993 observation to the 1995 one for both hard and soft components, regardless of the model combination. Anyway, SN 1978K shows spectral parameters similar to those of the north-arm SNR in NGC 6946.

SN 1986J As already mentioned in § 4.2, three *ROSAT* and two *ASCA* observations were already reported by Houck et al. (1998). Here we analyze only the *ASCA* data.

For both 1994 and 1996 observations, we extracted the source spectrum from a $3'$ radius region. The R-S model provide the lowest value of χ^2 for both the 1994 and 1996 observations among our single component models, and can represent the Fe-line feature seen in the spectra around 6.7 keV. This result confirms the analysis by Houck et al. (1998), although they performed more detailed spectral study.

In summary, all these three SNRs show spectral features different from ULXs we studied so far. None of our ULXs shows the $kT \sim 1$ keV soft thermal radiation observed from the north-arm SNR in NGC 6946 and SN 1978K, or the Fe-line emission as is seen in SN 1986J. Thus, we securely conclude that ULXs belong to a category which is different from luminous SNRs. In particular, none of our ULXs are likely to be unidentified SNRs. We have thus ruled out one of the scenarios (§ 2.5.3) explaining the ULXs.

(a) SNR in NGC 6946 (b) SN 1978K 95/11 (c) SN 1986J 96/4

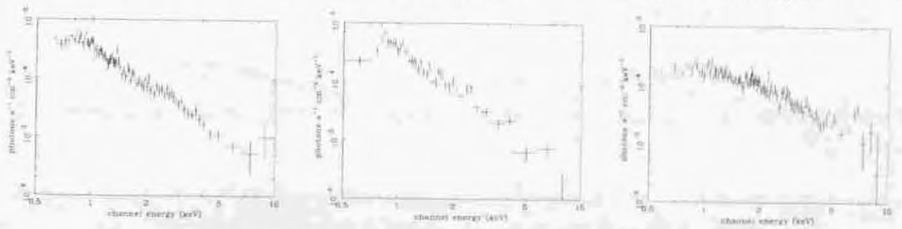

Figure 6.23: Unfolded SIS spectra of extragalactic SNRs.

6.10 Comparison of the Spectral Modelings

Among our single component models so far tested, the power-law model represents a straight line, the TBS model has a mildly convex continuum, and the MCD model has

Table 6.15: Fitting results of luminous extragalactic SNRs, using single component models.

Source	Model	$N_{\rm H}$ (10^{22}cm^{-2})	Parameters[a]	$f_{\rm X}$ [b] (0.5–10 keV)	χ^2/ν (confidence level)
North-arm source in NGC 6946					
	power-law	0.11±0.04	2.28±0.12	1.33	105.4/87 (9%)
	TBS	≤0.02	3.0±0.3	1.24	121.4/87 (1%)
	R-S	≤0.02	$3.0\pm0.3/0.03^{+0.11}_{-0.03}$	1.25	121.1/86 (1%)
	MCD	0	0.84	1.05	210.4/87 (≤1%)
SN 1978K in 1993 Jul.					
	power-law	0.12±0.06	2.31±0.16	1.28	33.9/44 (86%)
	TBS	≤0.03	3.0±0.5	1.38	45.1/44 (42%)
	R-S	≤0.03	$3.0\pm0.5/0.17^{+0.27}_{-0.17}$	1.39	43.7/43 (44%)
	MCD	≤0.01	0.86±0.08	1.13	85.3/44 (≤1%)
in 1995 Nov.					
	power-law	0.24±0.05	2.51±0.16	1.21	119.1/68 (≤1%)
	TBS	0.08±0.04	2.6±0.4	1.14	134.6/68 (≤1%)
	R-S	0.08±0.04	$2.7\pm0.4/0.21^{+0.25}_{-0.21}$	1.15	129.9/67 (15%)
	MCD	0	0.91	1.03	164.9/68 (≤1%)
SN 1986J in 1994 Jan.					
	power-law	0.26±0.07	1.55±0.08	2.28	170.4/138 (3%)
	TBS	0.19±0.05	$15.6^{+6.1}_{-4.5}$	2.20	170.5/138 (3%)
	R-S	0.23≤0.06	$10.3^{+3.1}_{-1.9}/1.0^{+0.48}_{-0.38}$	2.26	153.2/137 (16%)
	MCD	≤0.05	2.13±0.16	2.11	191.2/138 (≤1%)
in 1996 Jan.					
	power-law	0.26±0.06	1.71±0.08	1.80	196.8/189 (33%)
	TBS	0.17±0.04	$8.7^{+2.1}_{-1.5}$	1.73	196.5/189 (34%)
	R-S	0.18±0.05	$7.6\pm0.8/0.76^{+0.34}_{-0.29}$	1.79	175.5/188 (73%)
	MCD	0.03±0.03	1.71±0.12	1.59	219.9/189 (6%)

[a] Photon index for the power-law model, plasma temperature (keV) for the TBS model, kT (keV)/abundance (solar) for the R-S model, and $T_{\rm in}$ for the MCD model.
[b] In unit of 10^{-12} erg s^{-1} cm^{-2}.

Table 6.16: Fitting results of luminous extragalactic SNRs, using double component models.

Source	Model	$N_{\rm H}$ (10^{22}cm^{-2})	Γ or kT (keV)	$f_{\rm X}^{\rm hard}$ [a] (0.5–10 keV)	kT (keV)/ Abundance(solar)	$f_{\rm X}^{\rm soft}$ [a] (0.5–10 keV)	χ^2/ν (confidence lev
North-arm SNR in NGC 6946							
	power-law+R-S	0.14±0.06	2.11±0.14	1.20	$0.83\pm0.07/0.63^{+0.24}_{-0.18}$	0.13	73.5/84 (78%
	TBS+R-S	0.09±0.07	$4.8^{+4.0}_{-1.4}$	1.01	$0.84\pm0.07/0.11^{+0.11}_{-0.07}$	0.28	72.6/84 (81%
SN 1978K in 1993 Jul.							
	power-law+R-S	0.14±0.04	2.24±0.16	1.40	0.80(fix)/1.20(fix)	0.09	29.6/43 (94%
	TBS+R-S	0.04≤0.1	3.8±0.9	1.24	0.82(fix)/0.25(fix)	0.18	34.5/43 (82%
1995 Nov.							
	power-law+R-S	0.35±0.12	2.24±0.20	1.01	$0.79\pm0.09/1.20^{+0.89}_{-0.55}$	0.23	76.8/65 (15%
	TBS+R-S	0.28±0.14	3.9±1.0	0.88	0.81±0.09/0.25≥0.08	0.31	75.2/65 (18%

[a] In unit of 10^{-12} erg s^{-1} cm^{-2}.

(a) North-arm SNR in NGC 6946 Power-law

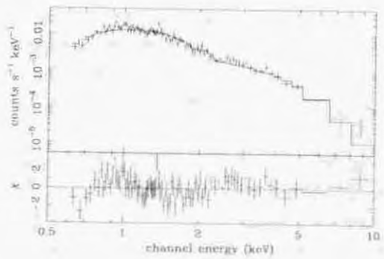

(b) North-arm SNR in NGX 6946 Power-law + R-S

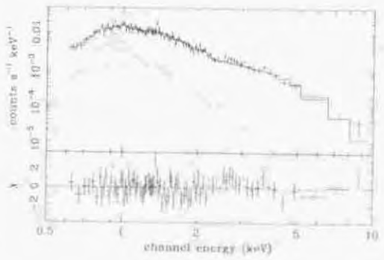

(c) SN 1978K 93/07

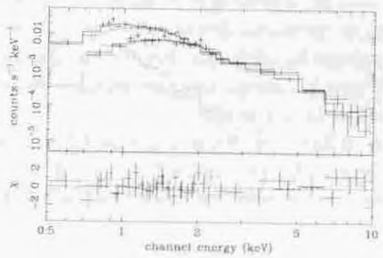

(d) SN 1978K 95/11

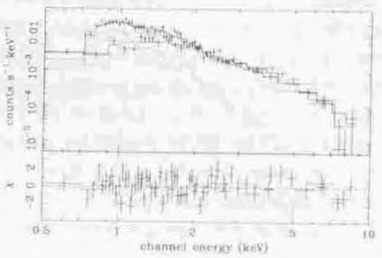

(e) SN 1986J 94/01

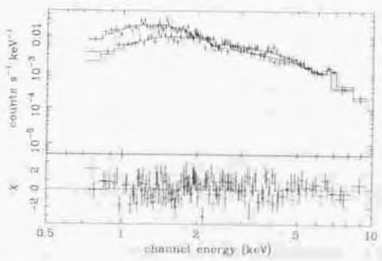

(e) SN 1986J 96/01

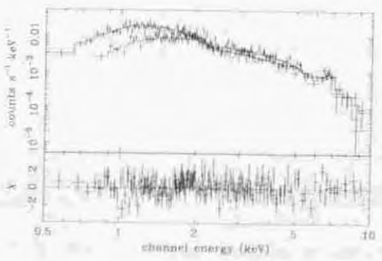

Figure 6.24: The background-subtracted spectra of luminous extragalactic SNRs. When using double component models, the contribution of each component is indicated by dotted lines. The spectra of SN 1978K are fitted with a power-law plus R-S model, and those of SN 1986J are fitted with a single R-S model.

the most convex shape in the logalithmic plot. We end this chapter by comparing these three models based on the χ^2 goodness and the values of absorption.

Figure 6.25 compares χ^2/ν between the power-law and MCD models, or between the TBS and MCD models. For the sources which were observed twice, we plotted results from the first observation for simplicity. The data points for M81 X-6 refer to the high-temperature state. Except for NGC 1313 source A, the MCD fit thus gives systematically lower values of χ^2/ν to the ULX spectra than the power-law fit, while the three SNRs exhibit the opposite tendency. The same statement applies to the comparison between the TBS and MCD modelings, though less significant.

Figure 6.26 provides a comparison of the models in terms of the absorption they require, where we plotted only the ULXs. We also excluded M33 X-8 and NGC 1313 source A, since the former showed different values of $N_{\rm H}$ between the SIS and the GIS, and for the latter we fixed the absorption when performed spectral fitting. The values of $N_{\rm H}$ associated with the power-law fits largely exceed the Galactic $N_{\rm H}$, and take rather constant values at $(0.4-1)\times10^{22}$ cm^{-2}. The TBS fits show similar excess in $N_{\rm H}$, although less prominent than the power-law fits. Of course, the ULXs may exhibit self-absorption, but in that case, the excess $N_{\rm H}$ would scatter from object to object, just as is seen from X-ray pulsars. Therefore the excess absorption can be considered as an artifact required to make the models more convex than they are. In contrast, the values of $N_{\rm H}$ associated with the MCD fits are closer to the Galactic values In addition, the excess $N_{\rm H}$ in this case scatters randomly up to several times 10^{21}cm^{-2}. These may be attributed to the absorption intrinsic to the ULXs, or internal to the host galaxies.

In summary, the MCD modeling can give a unified description of the ULX spectra, except a few cases; the M33 X-8 spectra and the 1995 spectra of NGC 1313 source A require the additional hard power-law, while the 1993 spectra of the same source A and IC 342 source 2 prefer a single power-law.

(a) Power-law vs. MCD

(b) TBS vs. MCD

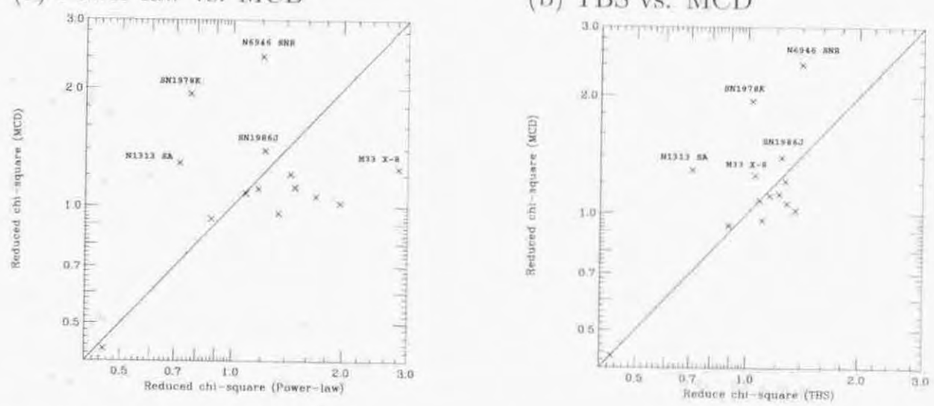

Figure 6.25: A comparison of the obtained χ^2/ν between the power-law model and the MCD one (panel a), and between the TBS model and the MCD one (panel b). For the objects observed twice, we plotted the results of the first observation, and for M81 X-6, we plotted the values obtained for the high-temperature state spectrum.

(a) Power-law (b) TBS (c) MCD

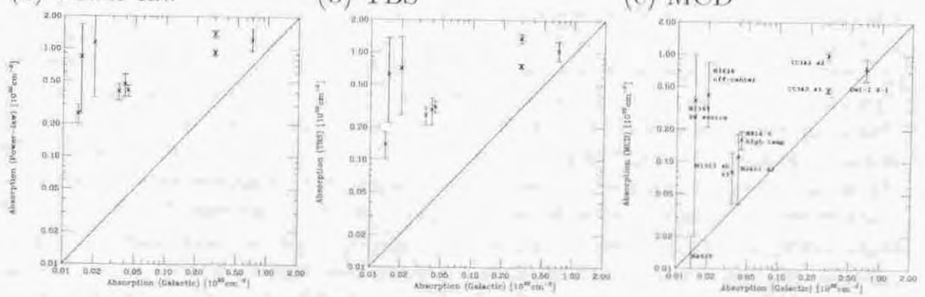

Figure 6.26: Summary of the obtained values of $N_{\rm H}$ for the single component models, in comparison with the Galactic line-of-sight $N_{\rm H}$. The results of the power-law (panel a), the TBS (panel b), and the MCD model (panel c) are plotted. NGC 1313 source A, M33 X-8, and three SNRs are excluded (see text).